

Beyond Degradation Redundancy: Contrastive Prompt Learning for All-in-One Image Restoration

Gang Wu, *Student Member, IEEE*, Junjun Jiang[✉], *Senior Member, IEEE*, Kui Jiang, *Member, IEEE*, Xianming Liu, *Member, IEEE* and Liqiang Nie, *Senior Member, IEEE*

arXiv:2504.09973v3 [cs.CV] 30 Dec 2025

Abstract—All-in-One Image Restoration (AiOIR), which addresses diverse degradation types with a unified model, presents significant challenges in designing task-aware prompts that effectively guide restoration across multiple degradation scenarios. While adaptive prompt learning enables end-to-end optimization, it often yields overlapping or redundant task representations. Conversely, explicit prompts derived from pretrained classifiers enhance discriminability but discard critical visual information needed for reconstruction. To address these limitations, we introduce Contrastive Prompt Learning (CPL), a framework that aims to improve prompt-task alignment through two complementary components: a Sparse Prompt Module (SPM) that efficiently captures degradation-aware representations while reducing redundancy, and a Contrastive Prompt Regularization (CPR) that explicitly strengthens task boundaries by incorporating negative prompt samples across different degradation types. Unlike previous approaches that focus primarily on degradation classification, CPL directly optimizes the interaction between prompts and the restoration model. Extensive experiments across five benchmarks show that CPL consistently boosts the performance of strong AiOIR baselines across diverse scenarios. Our approach achieves state-of-the-art average performance on these benchmarks, providing a general and robust solution for AiOIR. The code is available at <https://github.com/Aitical/CPLIR>

Index Terms—Image Restoration, Prompt Learning, Contrastive Learning, Image Deraining, Image Dehazing, Image Denoising

I. INTRODUCTION

Image restoration (IR) has long been a core problem in low-level computer vision, focusing on recovering high-quality images from degraded observations [1], [2]. Common image degradations, such as noise, blur, haze, rain, and poor illumination make image restoration a diverse and specialized field. To address these challenges, researchers have developed tailored solutions for each degradation type, with methods optimized for specific image artifacts [3]–[7]. While these

The research was supported by the National Natural Science Foundation of China (62471158, U23B2009) and the Natural Science Foundation of Heilongjiang Province of China for Excellent Youth Project (YQ2024F006).

G. Wu, J. Jiang, K. Jiang, and X. Liu are with the School of Computer Science and Technology, Harbin Institute of Technology, Harbin 150001, China. E-mail: {gwu@hit.edu.cn, jiangjunjun@hit.edu.cn, jiangkui@hit.edu.cn, csxm@hit.edu.cn}. Corresponding author: Junjun Jiang.

L. Nie is with the School of Computer Science and Technology, Harbin Institute of Technology (Shenzhen), Shenzhen 518055, China. E-mail: {nieliqiang@gmail.com}.

Copyright (c) 2013 IEEE. Personal use of this material is permitted. However, permission to use this material for any other purposes must be obtained from the IEEE by sending a request to pubs-permissions@ieee.org.

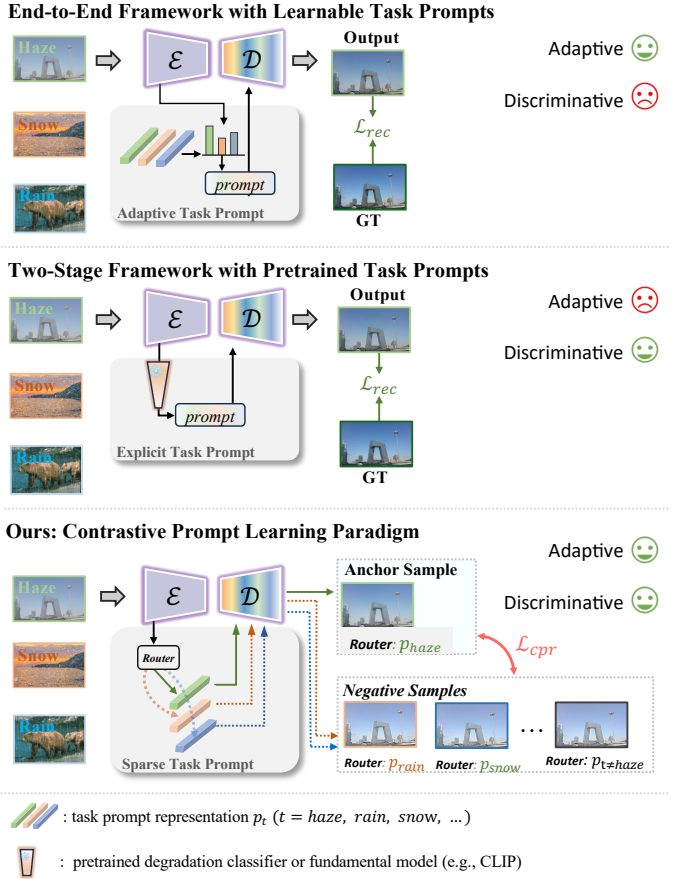


Fig. 1. Comparison of prompt-based AiOIR frameworks. (a) Adaptive end-to-end learnable prompts. (b) Two-stage frameworks with pretrained degradation encoders. (c) The proposed CPL paradigm with sparse prompt selection and CPR.

methods excel in their respective tasks, their practical utility remains limited. Real-world images are often corrupted by unknown or multiple interacting degradations, demanding a more versatile solution. This has spurred the development of All-in-One Image Restoration (AiOIR) approaches [8], which strive to handle a broad spectrum of degradations within a single unified model.

A common strategy for enabling such versatility is the use of task-aware prompts, which provide the model with additional guidance for tackling different degradations. Research in this area has diverged into two dominant paradigms, each with inherent limitations. The first paradigm, *adaptive prompt learning* [9]–[11], learns prompts jointly with the restoration

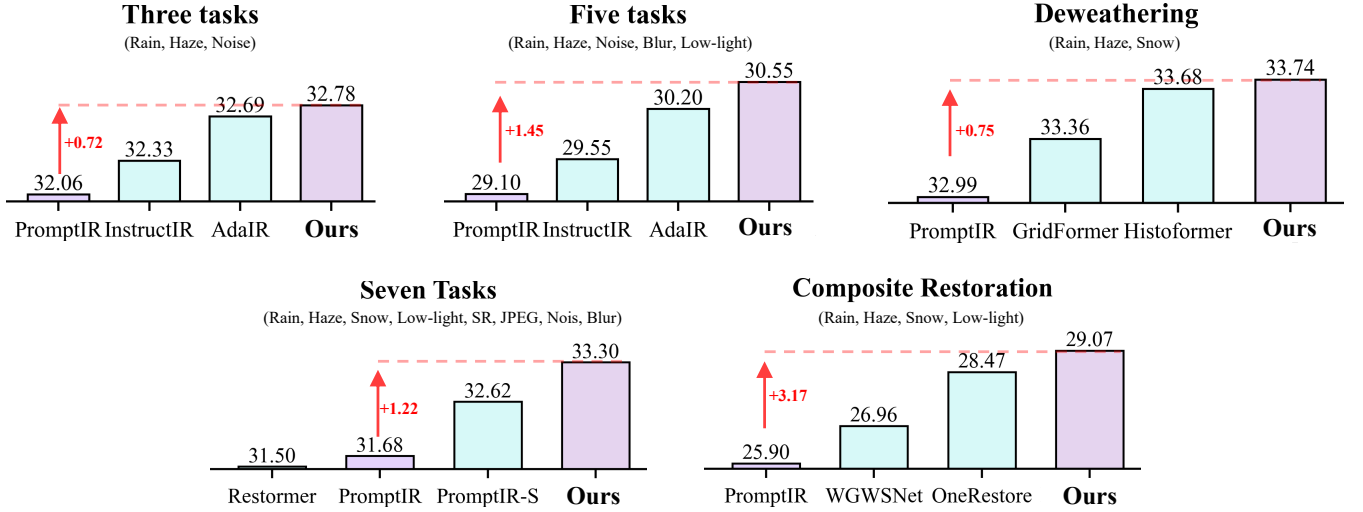


Fig. 2. Performance comparison. Integrating our CPL framework into existing all-in-one models improves performance across various tasks in our experiments.

network in an end-to-end manner. While offering flexibility, this approach often leads to prompts with high *representation redundancy*, where task-specific information becomes entangled and ambiguous. The second paradigm is *explicit prompt learning* [12]–[14], which leverages pretrained classifiers to generate highly discriminative degradation features. However, this emphasis on discriminability can lead to *functional misalignment*, as features that are optimized for classification are not necessarily optimal for the nuanced task of high-fidelity image reconstruction [13].

While these advancements have enabled all-in-one frameworks to handle multiple degradation tasks, several issues remain. Based on existing research [9], [10], [12]–[14], task prompts are crucial for AiOIR and are typically obtained through either adaptive or explicit learning. A crucial challenge stems from the inherent commonalities across degradation tasks. For instance, dehazing and low-light enhancement share global illumination patterns, while rain removal and denoising involve similar texture statistics [15], [16]. These shared characteristics make it difficult for adaptive learning approaches, where prompts are learned jointly with the restoration model [9]–[11], to develop clearly separated task representations. This redundancy is quantitatively evident in PromptIR [10], which uses a softmax function to ensemble multiple task-oriented prompts and yields a relatively dense probability distribution. To measure this redundancy, we calculate the Shannon entropy of the softmax probability distribution over different task prompts during inference. Lower entropy values approaching zero indicate that the model clearly distinguishes between tasks, while higher values suggest overlapping representations where multiple prompts are activated simultaneously. Our analysis shows relatively high entropy values: 2.23 bits for rain, 2.08 bits for haze, and approximately 2.24 bits for noise levels 15, 25, and 50, indicating that the learned prompts exhibit limited task specificity. Alternatively, explicit prompt learning approaches employ a two-stage strategy with a pre-trained degradation classifier [12]–[14] to yield more discriminative representations. However, recent studies [13]

have reported that highly discriminative features optimized for classification do not always translate into improved restoration quality, suggesting a misalignment between obtaining discriminative prompts and the requirements of the restoration model. In essence, adaptive methods tend to produce redundant prompts, while explicit methods can produce discriminative but potentially misaligned prompts. This brings us to a central question: *How can we design prompts with sufficient discriminative power while preserving the fine-grained information required by the restoration model?*

In this paper, we propose *Contrastive Prompt Learning* (CPL), a paradigm that addresses the above dilemma through two complementary perspectives. To combat *representation redundancy*, we introduce a SPM. Specifically, we employ a sparse selection mechanism for prompt representations to enhance the intrinsic quality and expressive power of each individual prompt. As illustrated in Figure 1, it connects adaptive and explicit learning paradigms through a sparse gated router, which derives degradation representations from dense, parameterized prompts. Moreover, to alleviate *functional misalignment*, we propose the CPR. Instead of constraining the prompt embeddings directly, CPR introduces a *model-prompt decoupling strategy* that regularizes the final restoration outcome. By treating mismatched prompt-model pairings as negative samples, CPR directly optimizes the *functional behavior* of the prompts, encouraging them to align with the goal of high-quality reconstruction. This mechanism penalizes the restoration model when prompts are incorrectly assigned to degradations, thereby establishing clearer associations between specific prompt representations and their corresponding degradation types.

By striking a balance between discriminative power and reconstruction quality, our CPL framework reduces cross-task confusion while preserving the information required for high-quality image restoration. As a result, the learned prompts become more task-consistent and better aligned with the underlying degradation characteristics. We conduct extensive experiments on a wide range of AiOIR benchmarks. As

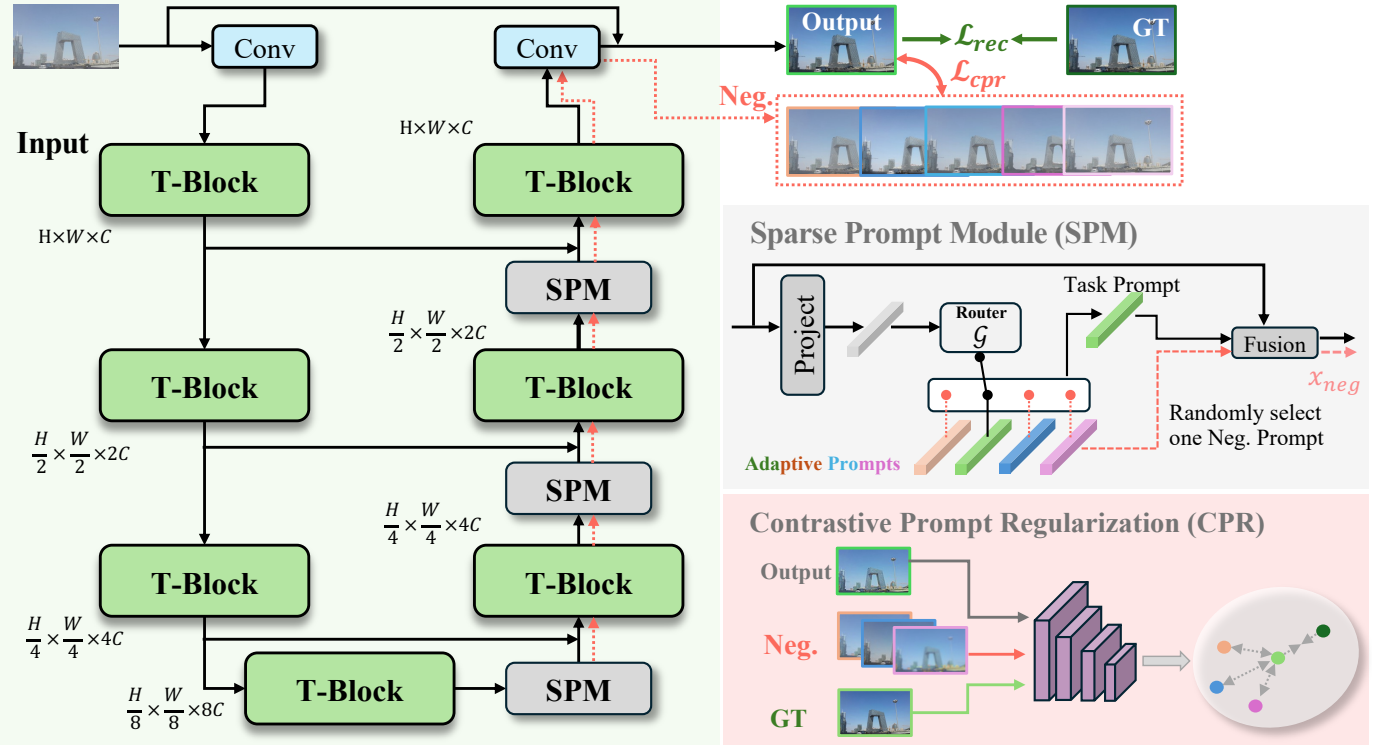


Fig. 3. Illustration of the proposed CPL framework with the SPM and CPR. We adopt a stacked Transformer block (T-Block) backbone following [10]. Red dashed arrows denote the generation of negative samples used only during training.

illustrated in Figure 2, CPL advances the performance of baseline models and attains strong results across all evaluated configurations. Our main contributions are as follows:

- We reveal and quantify the critical issues of *representation redundancy* and *functional misalignment* in current AiOIR frameworks.
- We propose a SPM that leverages principled sparsity to enhance the intrinsic quality and expressive power of prompt representations, effectively mitigating redundancy.
- We introduce CPR, a novel functional regularization paradigm that aligns prompts with the restoration objective through a model-prompt decoupling strategy, a clear departure from standard contrastive learning.
- We demonstrate the effectiveness and flexibility of our method through extensive experiments, consistently improving performance across multiple datasets with complex, mixed degradations.

The rest of the paper is organized as follows: Section II reviews related work on both single-task and AiOIR, along with prompt-based learning and contrastive learning methods in computer vision. Section III provides the technical details of our CPL. Section IV presents experimental results, demonstrating how our framework alleviates prompt misalignment and achieves competitive performance on various benchmarks. Finally, Section V summarizes our main findings and discusses potential future research directions for further enhancing prompt-based AiOIR.

II. RELATED WORK

A. Single-Task Image Restoration

Image restoration is a foundational task in computer vision, aiming to recover high-quality images from degraded inputs affected by various distortions [2]. With the rapid advancement of deep learning techniques, substantial progress has been achieved in addressing single degradation tasks, where specialized algorithms are developed for specific degradation types, such as image denoising [17], [18], deblurring [4], [19]–[22], dehazing [23], [23]–[26], deraining [5], [27]–[31], and low-light enhancement [7], [32]–[35]. Beyond these task-specific approaches, several general restoration architectures have emerged that provide strong baseline performance across multiple tasks [21], [36]–[42], together with diffusion-based architectures [43]–[46]. While the above task-specific methods have achieved strong results, their limited ability to generalize across different degradation types restricts their practicality in real-world applications, where images frequently suffer from multiple or unknown degradations simultaneously. To address this limitation, recent research has shifted towards developing AiOIR frameworks capable of handling multiple degradation types within a unified model [8].

B. All-in-One Image Restoration

Recent approaches introduce task-aware prompts or conditioning mechanisms to better differentiate between degradation types. AirNet [9] proposed a dedicated degradation encoder to extract degradation-specific features, enabling adaptive restoration across various tasks. Building on this foundation,

PromptIR [10] integrated learnable prompt components during the decoding stage to inject task-related information, improving the model's flexibility and performance. The evolution of AiOIR has proceeded along two primary trajectories. The first focuses on improving learnable task prompts through additional prior regularization techniques, such as frequency analysis in AdaIR [11] and principal component analysis in [47]. These approaches aim to enhance the discriminative power of task representations while maintaining their relevance to restoration objectives.

The second trajectory leverages predefined degradation priors with explicit prompt learning. MioIR [12] introduced a sequential learning strategy, effectively capturing task-specific characteristics through a pretrained degradation classifier. This explicit approach has gained significant attention due to its effectiveness in providing clear degradation signals. Further extending this concept, several studies have incorporated pretrained vision-language models (VLMs) like CLIP [48] to inject semantic information into the restoration process [13], [49], [50]. By utilizing textual descriptions or embeddings, these methods provide additional contextual guidance that aids in reconstructing images with complex degradations. In addition, some works focus on the optimization of AiOIR, introducing multi-task learning approaches [51], [52] and masked image pretraining [53]. Despite significant advancements, existing all-in-one methods are hindered by two critical issues: representation redundancy and prompt-task misalignment. The lack of explicit constraints in adaptive learning often leads to ambiguous, overlapping prompts that degrade performance. To address this, we introduce the SPM, a solution that enhances prompt quality through principled sparse selection. Our approach offers a distinct advantage in its integration efficiency; it can be seamlessly incorporated into existing adaptive frameworks with minimal architectural overhead. Furthermore, while our method shares conceptual similarities with Mixture-of-Experts (MoE) architectures [54], the underlying motivation is notably different. Classical MoE primarily employs conditional computation to achieve architectural scalability, i.e., to increase backbone capacity without a proportional increase in computational cost. In contrast, we leverage sparsity as a structural prior for *prompt representation* learning. By enforcing sparse selection among prompt modules, the model is encouraged to let each prompt specialize on a subset of degradations, which in turn reduces overlap between prompts and mitigates the feature redundancy observed in dense prompt ensembles.

C. Contrastive Learning in Low-Level Image Restoration

Contrastive learning has emerged as a powerful paradigm in self-supervised representation learning, enabling models to learn discriminative features by contrasting positive and negative sample pairs [55]. In recent years, researchers have increasingly adapted contrastive learning principles to address the unique challenges of low-level image restoration tasks [56]–[62]. Unlike high-level vision, where semantic feature discrimination is paramount, restoration tasks require preserving fine-grained details while removing task-specific

degradations. This leads to specialized contrastive frameworks across various restoration domains. For image dehazing, Wu *et al.* [56] pioneered the application of contrastive regularization by treating low-quality inputs as negative samples, while Zheng *et al.* [57] advanced this approach through progressive negative sample selection within a continual learning framework. In the super-resolution task, Wu *et al.* introduced PCL [58], a practical contrastive learning framework that incorporates hard negative sample construction to better distinguish fine-grained frequency patterns.

The contrastive paradigm has been further extended to other restoration tasks with domain-specific adaptations. For image deraining, Ran *et al.* [59] developed contrastive regularization that leverages the decoupled representations of rain masks and background content to enhance separation. Chang *et al.* [60] proposed an unsupervised deraining method using asymmetric non-local contrastive learning, leveraging intra-layer self-similarity and inter-layer exclusiveness to effectively distinguish rain from clean images without supervision. Gao *et al.* [61] proposed FADFormer, which introduces a frequency-aware contrastive loss that operates in the frequency domain to better capture structural degradations. Moving toward more general image restoration frameworks, Wu *et al.* [62] introduced a task-agnostic model contrastive learning paradigm that simplifies negative sample construction while maintaining effectiveness across different degradation types. Despite these significant advances, existing contrastive learning approaches in low-level vision remain predominantly designed for single-task scenarios, focusing on enhancing feature representations for specific degradation types. They do not address the unique challenges presented by multi-task or AiOIR frameworks, particularly the potential misalignment issues arising from task-oriented prompts that must seamlessly coordinate multiple restoration objectives simultaneously.

While conventional contrastive methods in low-level vision primarily focus on enhancing feature discrimination within a single degradation context, our work introduces a conceptual shift in applying contrastive learning to this domain. Rather than directly constraining the prompt embeddings, a strategy that risks misaligning them with the reconstruction goal, our CPR targets the functional outcome of the restoration process. The key innovation is a *prompt-model decoupling* strategy, where negative samples are generated from mismatched prompt-model pairings. This directly regularizes the prompt's functional alignment with the model, ensuring it is optimized for reconstruction quality over mere classification.

III. METHOD

In this section, we present the Contrastive Prompt Learning (CPL) framework for AiOIR. We address the core challenges of representation redundancy and prompt-task misalignment through two complementary mechanisms. First, the SPM enhances the intrinsic quality of prompts by fostering representation specialization through sparse selection. Second, the *Contrastive Prompt Regularization* (CPR) strategy ensures that these specialized prompts are optimally utilized by enforcing functional alignment between the prompt guidance and the

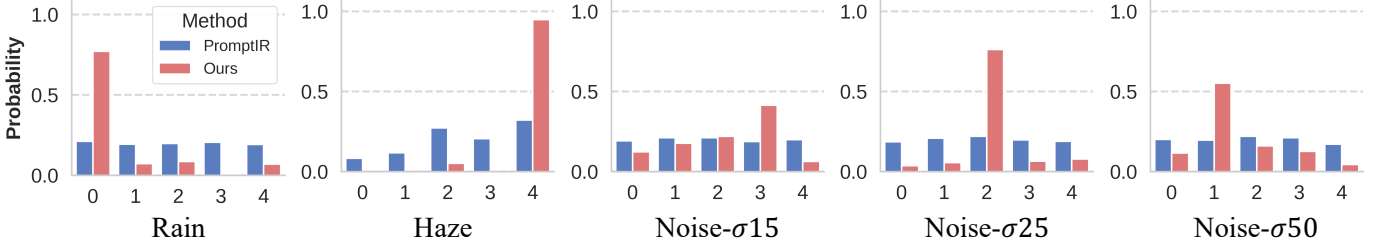


Fig. 4. Comparison of prompt selection probability distributions between baseline PromptIR [10] and CPL across different degradation tasks. The x-axis (0–4) denotes prompt indices and the y-axis denotes selection probabilities. PromptIR (blue) activates multiple prompts for a given task, whereas CPL (red) produces more concentrated, task-specific prompt selections.

restoration backbone’s behavior. The overall framework is illustrated in Figure 3.

A. Preliminaries

AiOIR aims to address various degradation types (e.g., denoising, deblurring, dehazing, deraining, low-light enhancement) within a unified model. Let $t \in \mathcal{T}$ denote a specific degradation type, and let \mathbf{I}_d be the degraded input image. In prompt-based approaches, each task t is associated with a learned prompt \mathbf{p}_t that guides the restoration process. The restoration model, parameterized by θ , can be formulated as:

$$\mathbf{I}_r = \mathcal{F}(\mathbf{I}_d, \mathbf{p}_t; \theta), \quad (1)$$

where \mathbf{I}_r is the restored image. The prompt \mathbf{p}_t should provide distinct, task-specific guidance to remove artifacts associated with task t , ensuring that \mathbf{I}_r closely approximates the ground truth \mathbf{I}_{gt} .

However, standard adaptive approaches often suffer from *prompt-task misalignment* [10], where the learned prompts fail to provide distinct task information. As evidenced by the entropy analysis in Figure 4, baseline methods (e.g., PromptIR) exhibit elevated entropy values (2.08–2.24 bits) across degradation types, indicating significant overlap between task representations. This redundancy stems from two limitations: (1) the softmax-based selection mechanism often yields diffuse probability distributions rather than selecting a dominant, task-specific expert; and (2) the optimization objective focuses solely on reconstruction, lacking explicit constraints to enforce prompt discriminability. Our CPL framework addresses these issues directly. As shown in Figure 4, our method achieves highly concentrated distributions. By combining sparse prompt selection with contrastive regularization, we establish clearer boundaries between task representations while strengthening their alignment with the restoration process.

B. Sparse Prompt Module

To mitigate representation redundancy, we introduce the SPM. Unlike conventional approaches that learn dense, entangled prompt representations, SPM employs a dynamic gating mechanism to selectively activate prompts based on the input. This compels each individual prompt expert to develop a more specialized and expressive representation.

1) *Module Architecture*: The SPM comprises two key components: (1) a set of n learnable prompt experts $\{\mathcal{E}_1, \mathcal{E}_2, \dots, \mathcal{E}_n\}$, each encoding distinct degradation priors, and (2) a gating network \mathcal{G} that determines the contribution of each expert. Given input features \mathbf{x} extracted from the degraded image \mathbf{I}_d , the SPM generates the prompt \mathbf{p} as follows:

$$\mathbf{p} = \sum_{i=1}^n g_i(\mathbf{x}) \cdot \mathcal{E}_i(\mathbf{x}), \quad (2)$$

where \mathbf{p} represents the generated task prompt, $\mathcal{E}_i(\mathbf{x})$ is the output of the i -th prompt expert, and $g_i(\mathbf{x})$ is the gating weight for expert i computed by the gating network \mathcal{G} .

2) *Sparse Gating Mechanism*: To enforce specialization, we employ a top- k sparse gating mechanism to activate the most relevant prompts. The gating weights are computed by:

$$\mathcal{G}(\mathbf{x}) = \text{top-}k(\text{softmax}(W_g \mathbf{x} + b_g), k), \quad (3)$$

where W_g and b_g are learnable parameters. The top- k operator retains the k largest values from the softmax distribution and sets the rest to zero, re-normalizing the active weights to sum to one. This sparsity constraint offers two advantages. First, it acts as a regularization term that reduces representational overlap, as prompts must compete to be selected for specific degradation patterns. Second, it improves computational efficiency by activating only a subset of prompts (typically $k \ll n$) during inference, while still allowing the model to learn from a diverse pool of prompts during training.

C. Contrastive Prompt Regularization

While SPM improves the intrinsic discriminability of the prompts, there remains a risk of *functional misalignment*: a prompt might be distinct in the embedding space but fail to trigger the correct restoration behavior in the IR backbone. To address this, we introduce the CPR. Conventional contrastive learning typically operates on the feature embeddings. However, in low-level restoration, embedding-level discrimination does not guarantee optimal reconstruction. Therefore, CPR shifts the regularization target from the latent representation to the corresponding output of the model. We propose the *model-prompt decoupling concept* that penalizes the model when it produces high-quality results with incorrect prompts, thereby enforcing a strict dependency between the prompt guidance and the restoration outcome.

Algorithm 1 CPR for AiOIR

Require: Training set $\mathcal{D} = \{(\mathbf{I}_d, \mathbf{I}_{gt}, t)\}$; prompts $\{\mathbf{p}_t\}$; model $\mathcal{F}(\cdot; \theta)$; hyperparameter α .

- 1: Initialize model parameters θ .
- 2: **for** each training iteration **do**
- 3: Sample a batch $\{(\mathbf{I}_d, \mathbf{I}_{gt}, t)\}$ from \mathcal{D} .
- 4: **for** each sample in the batch **do**
- 5: **Positive Reconstruction:** $\mathbf{I}_r^+ = \mathcal{F}(\mathbf{I}_d, \mathbf{p}_t; \theta)$
- 6: **Negative Reconstructions:**
- 7: **for** each of m randomly chosen prompts $t' \neq t$ **do**
- 8: $\mathbf{I}_r^- = \mathcal{F}(\mathbf{I}_d, \mathbf{p}_{t'}; \theta)$
- 9: **end for**
- 10: Compute \mathcal{L}_{pos} using Eq. (4)
- 11: Compute \mathcal{L}_{neg} using Eq. (5)
- 12: $\mathcal{L}_{\text{cpr}} \leftarrow \mathcal{L}_{\text{pos}} - \mathcal{L}_{\text{neg}}$
- 13: $\mathcal{L}_{\text{pixel}} \leftarrow \|\mathbf{I}_r^+ - \mathbf{I}_{gt}\|_1$
- 14: $\mathcal{L} \leftarrow \mathcal{L}_{\text{pixel}} + \alpha \mathcal{L}_{\text{cpr}}$
- 15: **end for**
- 16: Back-propagate and update θ with $\nabla \mathcal{L}$.
- 17: **end for**
- 18: **return** θ

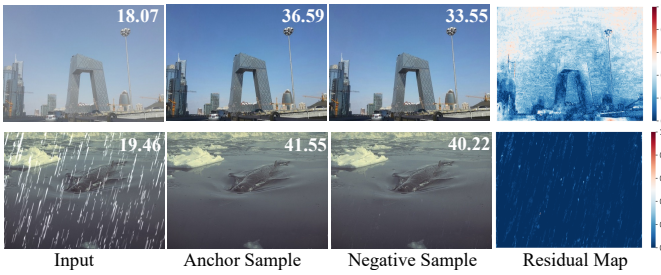


Fig. 5. Residual analysis for CPR. PSNR values are shown in the top-right corner of each image. Top row: haze example. Bottom row: rain example. Residual maps highlight differences between reconstructions obtained with matched and mismatched prompts.

1) *Functional Decoupling via Negative Prompting:* For a training sample $(\mathbf{I}_d, \mathbf{I}_{gt})$ associated with task t , we construct training pairs defined by their functional validity:

- **Positive Pairing (Matched):** The degraded image \mathbf{I}_d is paired with its corresponding prompt \mathbf{p}_t . The resulting output $\mathbf{I}_r^+ = \mathcal{F}(\mathbf{I}_d, \mathbf{p}_t; \theta)$ is optimized to match the ground truth.
- **Negative Pairing (Mismatched):** The same image \mathbf{I}_d is paired with a set of randomly sampled mismatched prompts $\mathbf{p}_{t'}$ (where $t' \neq t$). The resulting outputs $\mathbf{I}_r^- = \mathcal{F}(\mathbf{I}_d, \mathbf{p}_{t'}; \theta)$ serve as negative samples.

The core intuition is that if the restoration model \mathcal{F} is truly prompt-guided, feeding it a “dehazing” prompt for a “rainy” image should result in a failure to remove the rain (or an incorrect operation), leading to a representation distinct from the ground truth. If the model ignores the prompt and relies solely on image statistics, \mathbf{I}_r^- would resemble \mathbf{I}_r^+ , indicating a failure of prompt control.

2) *Contrastive Prompt Loss:* We adopt a pretrained VGG network denoted by $\phi(\cdot)$ to measure perceptual similarity in feature space. Let \mathbf{I}_{gt} be the ground-truth image. We formulate

two complementary loss terms:

a) *Positive Loss:* This term aims to reduce the distance between the positive reconstruction \mathbf{I}_r^+ and the ground truth \mathbf{I}_{gt} in feature space:

$$\mathcal{L}_{\text{pos}} = \|\phi(\mathbf{I}_r^+) - \phi(\mathbf{I}_{gt})\|_2^2. \quad (4)$$

b) *Negative Loss:* This term seeks to enlarge the distance between each negative reconstruction \mathbf{I}_r^- and \mathbf{I}_r^+ :

$$\mathcal{L}_{\text{neg}} = \frac{1}{|\mathcal{T}_t^-|} \sum_{t' \in \mathcal{T}_t^-} \|\phi(\mathbf{I}_{t'}^-) - \phi(\mathbf{I}_r^+)\|_2^2, \quad (5)$$

where \mathcal{T}_t^- denotes the set of m randomly sampled negative task types for the anchor task t . We combine these two terms into the *contrastive prompt Regularization loss*:

$$\mathcal{L}_{\text{cpr}} = \mathcal{L}_{\text{pos}} - \mathcal{L}_{\text{neg}}. \quad (6)$$

This encourages the model to produce high-quality outputs when using the correct prompt while degrading output quality when using incorrect prompts, effectively strengthening the functional boundary between different task prompts. Algorithm 1 details the training procedure for the proposed CPR approach. For each training sample, we generate both positive and negative reconstructions, compute the relevant losses, and update the model parameters accordingly.

3) *Overall Training Objective:* In addition to the contrastive prompt loss, we incorporate a standard ℓ_1 pixel-wise reconstruction term on the *positive* reconstruction:

$$\mathcal{L}_{\text{pixel}} = \|\mathbf{I}_r^+ - \mathbf{I}_{gt}\|_1. \quad (7)$$

Our final training objective is:

$$\mathcal{L} = \mathcal{L}_{\text{pixel}} + \alpha \mathcal{L}_{\text{cpr}}, \quad (8)$$

where α is a hyperparameter that controls how strongly the CPR is incorporated. By minimizing this combined loss, the model learns to produce high-quality restorations for matched (positive) prompts while simultaneously establishing clear boundaries between different task representations, effectively addressing both the discriminative power and alignment challenges identified in conventional prompt-based approaches.

D. Remark

The effectiveness of CPR is validated by our residual analysis in Figure 5. While reconstructions from positive and negative pairings may appear visually similar at a glance, the residual maps reveal critical, task-aware differences in their corresponding outcomes. For instance, in the haze example, the residual map highlights significant errors in global illumination patterns when an incorrect prompt is used. Similarly, for rain, the residual map clearly localizes errors to the rain-streak regions. This confirms that CPR successfully conditions the restoration model to be highly sensitive to the prompt’s semantic content, ensuring that the prompt acts as a genuine functional switch rather than a passive feature modulator.

TABLE I
QUANTITATIVE COMPARISON ON THE THREE-TASK AiOIR BENCHMARK. ASTERISKS (*) INDICATE RESULTS CITED FROM PRIOR WORK [10].

Type	Method	Venue	Denoising (CBSD68 [63])			Dehazing	Deraining	Average
			$\sigma = 15$	$\sigma = 25$	$\sigma = 50$	SOTS [64]	Rain100L [65]	
General	MPRNet [66]	CVPR'21	33.27/0.920	30.76/0.871	27.29/0.761	28.00/0.958	33.86/0.958	30.63/0.940
	Restormer [21]	CVPR'22	33.72/0.930	30.67/0.865	27.63/0.792	27.78/0.958	33.78/0.958	30.75/0.901
	NAFNet [36]	ECCV'22	33.03/0.918	30.47/0.865	27.12/0.754	24.11/0.928	33.64/0.956	29.67/0.844
	FSNet* [67]	TPAMI'23	33.81/0.930	30.84/0.872	27.69/0.792	29.14/0.968	35.61/0.969	31.42/0.906
	DRSformer* [68]	CVPR'23	33.28/0.921	30.55/0.862	27.58/0.786	29.02/0.968	35.89/0.970	31.26/0.902
	MambaIR* [40]	ECCV'24	33.88/0.931	30.95/0.874	27.74/0.793	29.57/0.970	35.42/0.969	31.51/0.907
All-in-One	DL [69]	TPAMI'19	33.05/0.914	30.41/0.861	26.90/0.740	26.92/0.391	32.62/0.931	29.98/0.875
	AirNet [9]	CVPR'22	33.92/0.932	31.26/0.888	28.00/0.797	27.94/0.962	34.90/0.967	31.20/0.910
	IDR* [47]	CVPR'23	33.89/0.931	31.32/0.884	28.04/0.798	29.87/0.970	36.03/0.971	31.83/0.911
	Gridformer* [39]	IJCV'24	33.93/0.931	31.37/0.887	28.11/0.801	30.37/0.970	37.15/0.972	32.19/0.912
	NDR [70]	TIP'24	34.01/0.932	31.36/0.887	28.10/0.798	28.64/0.962	35.42/0.969	31.51/0.910
	InstructIR [50]	ECCV'24	34.15/0.933	31.52/0.890	28.30/0.804	30.22/0.959	37.98/0.978	32.43/0.913
	TextualDegRemoval [49]	CVPR'24	34.01/0.933	31.39/0.890	28.18/0.802	31.63/0.980	37.58/0.979	32.63/0.917
	AdaIR [11]	ICLR'25	34.12/0.935	31.45/0.892	28.19/0.802	31.06/0.980	38.64/0.983	32.69/0.918
	PromptIR [10]	NeurIPS'23	33.98/0.933	31.31/0.888	28.06/0.799	30.58/0.974	36.37/0.972	32.06/0.913
PromptIR+CPL		2025	34.15/0.933	<u>31.50/0.889</u>	<u>28.23/0.800</u>	31.27/0.980	38.77/0.985	32.78/0.917

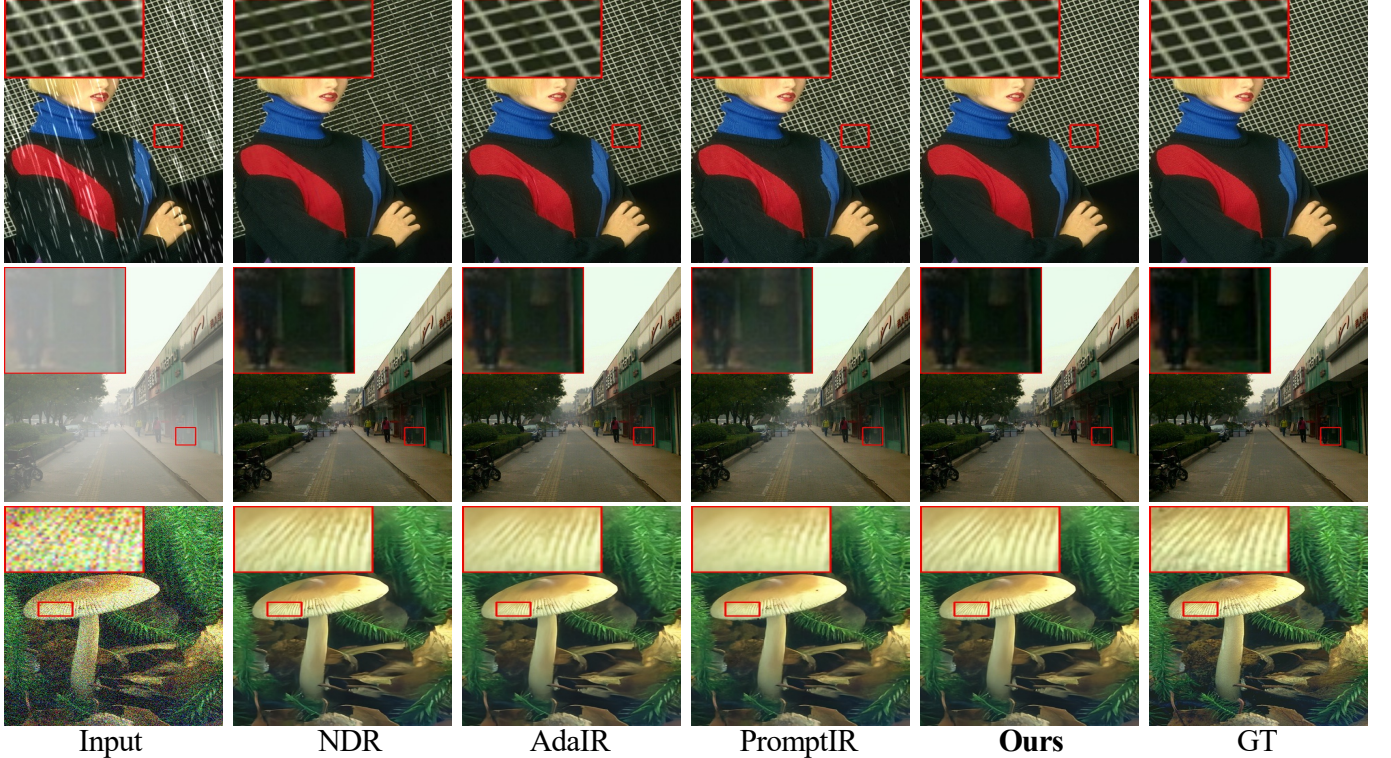


Fig. 6. Visual comparison on the three-task benchmark. CPL produces clearer structures, fewer residual artifacts, and better detail preservation compared with prior AiOIR methods.

IV. EXPERIMENTS

We evaluate the CPL framework across diverse AiOIR settings. We first outline the experimental setup and implementation details (Sec. IV-A, IV-B), followed by comparisons with state-of-the-art methods (Sec. IV-C). We then conduct ablation studies (Sec. IV-D) and conclude with limitations and future work (Sec. IV-E).

A. Experimental Setup

We evaluate CPL across several settings that cover both synthetic and real-world AiOIR scenarios:

- 1) **Three-task setting.** Following [9], [10], we evaluate image denoising, deraining, and dehazing. For denoising, we train on BSD400 [76] and WED [77] and test on CBSD68 [63] at noise levels $\sigma = 15, 25, 50$. For deraining, we use Rain100L [65], and for dehazing, we

TABLE II

QUANTITATIVE COMPARISON ON THE FIVE-TASK AiOIR BENCHMARK. ASTERISKS (*) INDICATE RESULTS CITED FROM PRIOR WORK [10], [70].

Type	Method	Venue	Denoising	Dehazing	Deraining	Deblurring	Low-light	Average
			CBSD68 [63]	SOTS [64]	Rain100L [65]	GoPro [71]	LOL [72]	
General	SwinIR [73]	ICCVW'21	30.59/0.868	21.50/0.891	30.78/0.923	24.52/0.773	17.81/0.723	25.04/0.835
	Restormer [21]	CVPR'22	<u>31.49</u> /0.884	24.09/0.927	34.81/0.962	27.22/0.829	20.41/0.806	27.60/0.881
	NAFNet [36]	ECCV'22	31.02/0.883	25.23/0.939	35.56/0.967	26.53/0.808	20.49/0.809	27.76/0.881
	DRSformer* [68]	CVPR'23	30.97/0.881	24.66/0.931	33.45/0.953	25.56/0.780	21.77/0.821	27.28/0.873
	Retinexformer* [32]	ICCV'23	30.84/0.880	24.81/0.933	32.68/0.940	25.09/0.779	22.76/0.834	27.24/0.873
	FSNet* [67]	TPAMI'23	31.33/0.883	25.53/0.943	36.07/0.968	28.32/0.869	22.29/0.829	28.71/0.898
	MambaIR* [40]	ECCV'24	31.41/0.884	25.81/0.944	36.55/0.971	28.61/0.875	22.49/0.832	28.97/0.901
All-in-One	DL [69]	TPAMI'19	23.09/0.745	20.54/0.826	21.96/0.762	19.86/0.672	19.83/0.712	21.05/0.743
	TAPE [74]	ECCV'22	30.18/0.855	22.16/0.861	29.67/0.904	24.47/0.763	18.97/0.621	25.09/0.801
	Transweather [75]	CVPR'22	29.00/0.841	21.32/0.885	29.43/0.905	25.12/0.757	21.21/0.792	25.22/0.836
	AirNet [9]	CVPR'22	30.91/0.882	21.04/0.884	32.98/0.951	24.35/0.781	18.18/0.735	25.49/0.846
	IDR [47]	CVPR'23	31.60 /0.887	25.24/0.943	35.63/0.965	27.87/0.846	21.34/0.826	28.34/0.893
	Gridformer* [39]	IJCV'24	31.45/0.885	26.79/0.951	36.61/0.971	<u>29.22</u> /0.884	22.59/0.831	29.33/0.904
	InstructIR [50]	ECCV'24	31.40/0.887	27.10/0.956	36.84/0.973	29.40 /0.886	<u>23.00</u> /0.836	29.55/0.907
	AdaIR [11]	ICLR'25	31.35/0.889	<u>30.53</u> /0.978	<u>38.02</u> /0.981	28.12/0.858	<u>23.00</u> /0.845	<u>30.20</u> /0.910
	PromptIR* [10]	NeurIPS'23	31.47/0.886	26.54/0.949	36.37/0.970	28.71/0.881	22.68/0.832	29.15/0.904
	PromptIR+CPL	2025	31.41/0.887	30.82 / 0.978	38.20 / 0.983	28.72/0.874	23.65 / 0.855	30.55 / 0.915

adopt the SOTS outdoor set from RESIDE [64].

- 2) **Five-task setting.** To evaluate broader task diversity, we follow [47] and consider denoising (CBSD68), dehazing (SOTS), deraining (Rain100L), motion deblurring (GoPro [71]), and low-light enhancement (LOL [72]). This configuration additionally includes motion deblurring and low-light enhancement compared to the three-task setting.
- 3) **Seven-task setting.** We adopt the protocol of [12], where images are synthesized from DF2K using seven degradations: super-resolution, blur, noise, JPEG compression, rain, haze, and low-light. This setting stresses the ability to handle many heterogeneous degradations within a single model.
- 4) **All-weather deweathering.** Following [75], we train on the AllWeather dataset [75], which contains samples from Raindrop [78], Outdoor-Rain [79], and Snow100K [80]. This setting evaluates AiOIR under diverse synthetic weather conditions.
- 5) **Real-world deweathering.** To assess generalization beyond synthetic data, we further evaluate on WeatherBench [81], a large-scale benchmark with 41,402 training and 600 test images captured under diverse real-world weather conditions (rain, haze, snow, and combinations thereof).
- 6) **Composite degradation setting.** To evaluate the model's generalization across complex degradation scenarios, we follow [82] and utilize the CDD-11 dataset, which is explicitly designed for composite degradations. CDD-11 is synthesized by applying eleven types of degradation (including haze, rain, snow, low-light, and their combinations) onto high-quality clear images using physically based rendering.

For all settings, we adopt baseline methods using the same

training/testing splits and protocols as in the original works to ensure a fair comparison. We then integrate the proposed CPL framework into these baselines to highlight the performance improvements driven by the CPL strategy. Unless otherwise specified, the best result in result table is highlighted in **bold**, and the second best is underlined.

B. Implementation Details

a) *Training Details:* All models are implemented in PyTorch and trained on two NVIDIA RTX 3090 GPUs. Unless otherwise specified, we use the Adam optimizer with an initial learning rate of 2×10^{-4} . We use a batch size of 8 and randomly crop 128×128 patches for training. Standard data augmentation, including random horizontal/vertical flips and 90° rotations, is applied.

b) *CPL Integration:* Specifically, we take PromptIR [10] as the default baseline and replace its prompt-selection component with our SPM. For each training sample, we generate multiple negative reconstructions using mismatched prompts to compute the CPR term. The VGG network used in CPR is kept fixed. The loss weight α in Eq. (8) is set to 0.01, unless otherwise noted in the ablation studies. For SPM, we use a top- k sparse gating mechanism. The number of active experts k is set to 1 by default, based on the ablation results in Sec. IV-D. During inference, only the selected experts contribute to the prompt, so the computational overhead is marginal.

C. Comparison with State-of-the-Art Methods

a) *Three-Task All-in-One Degradation Experiment:* Following established protocols [9], [10], we evaluate performance on denoising, deraining, and dehazing. Table I presents comparisons against specialized and all-in-one approaches.

TABLE III

QUANTITATIVE COMPARISON ON THE SEVEN-TASK AIOIR BENCHMARK. PROMPTIR VARIANTS ARE BASED ON THE RESTORMER BACKBONE WITH DIFFERENT TRAINING STRATEGIES: SEQUENTIAL LEARNING (S), EXPLICIT PROMPT LEARNING (EP), AND THE PROPOSED CPL.

Method	SR	Blur	Noise	JPEG	Rain	Haze	Low-Light	Avg.
SwinIR-S	26.02	31.58	31.36	33.40	36.69	29.58	34.64	31.90
Uformer-S	26.07	31.11	30.96	33.27	35.96	28.29	32.80	31.21
Restormer-S	25.95	31.55	30.86	33.24	38.06	25.48	36.69	31.69
Restormer+EP	25.82	31.87	30.94	33.17	36.22	26.60	40.37	32.14
PromptIR	25.86	31.46	30.75	33.07	35.76	26.62	39.62	31.88
PromptIR-S	26.14	32.02	31.08	33.43	39.97	27.21	38.46	32.62
PromptIR+CPL	26.22	32.24	31.28	33.61	40.91	28.29	40.55	33.30

The results demonstrate that CPL delivers consistent performance improvements when applied to existing architectures. Several key observations emerge: First, our model obtains an average PSNR of 32.78 dB, which is slightly higher than AdaIR [11] (32.69 dB). This gain suggests that our decoupling strategy effectively mitigates task interference that is common in all-in-one frameworks. Second, gains are pronounced for spatially complex degradations. For deraining, our approach achieves 38.77 dB PSNR (0.13 dB higher than AdaIR and 2.40 dB above the baseline PromptIR), while for dehazing, it delivers 31.27 dB. These improvements underscore the capability of CPL to capture spatially varying characteristics through adaptive feature extraction. Furthermore, Figure 6 provides visual comparisons. For denoising (bottom row), PromptIR+CPL recovers texture details (e.g., zebra stripes) while suppressing artifacts. In dehazing (middle row) and deraining (top row), our approach achieves superior color fidelity and structural preservation compared to baseline methods.

b) Five-Task All-in-One Degradation Experiment: To assess scalability, we extend the evaluation to a more diverse five-task benchmark, incorporating motion deblurring and low-light enhancement. As shown in Table II, our model achieves an average PSNR of 30.55 dB, outperforming the recent state-of-the-art AdaIR by 0.35 dB. A critical observation is the method’s robustness in handling distinct degradation mechanisms. Dehazing (veiling effect) and low-light enhancement (illumination recovery) involve global property shifts that differ significantly from additive noise removal. Relative to the PromptIR baseline, we observe improvements of +4.28 dB in dehazing and +0.97 dB in low-light enhancement, which can be attributed to our synergistic design. Specifically, the sparse prompt mechanism encourages individual prompts to acquire richer and more expressive representations by enforcing selection competition. In conjunction with CPR, this approach effectively decouples task-specific features while enhancing the degradation-aware information essential for the restoration model. This ensures that the model receives precise, non-conflicting guidance, thereby enabling it to accommodate diverse restoration objectives within a unified framework.

c) Seven-Task Comprehensive Evaluation: We conduct experiments on a comprehensive seven-task benchmark [12]. As shown in Table III, our approach achieves the highest average PSNR over all seven tasks, improving upon PromptIR-

S by 0.68 dB and upon the PromptIR baseline by 1.42 dB. These performance gains are consistent across all degradation types. When compared to other training strategies like sequential learning (S) and explicit prompt learning (EP), CPL consistently delivers superior results. For instance, while Restormer+EP performs well on low-light enhancement, it underperforms on other tasks. In contrast, PromptIR+CPL maintains robust performance across the full spectrum of degradations without compromising specific tasks, validating its effectiveness in mitigating task interference.

d) All-Weather Restoration Experiment: We evaluate our method on all-weather degradation scenarios [75], including snow, rain, and raindrops. As shown in Table IV, our approach achieves the best overall average performance, representing a 0.94 dB improvement over the original PromptIR and surpassing Histoformer [91] by 0.06 dB. Notably, our method demonstrates consistent gains across all datasets: 0.94 dB on Snow100K-S, 0.93 dB on Snow100K-L, 1.36 dB on Outdoor-Rain, and 0.53 dB on RainDrop. This balanced improvement supports CPL’s effectiveness in enhancing task-specific adaptation without compromising generalization capabilities. Figure 7 presents visual comparisons across different weather degradation types. For snow removal (first column), PromptIR+CPL completely eliminates snow particles while preserving intricate background details and natural colors. Other methods either leave snow residuals (TransWeather, WeatherDiff) or produce color distortions and over-smoothing (original PromptIR).

e) Real-World All-Weather Restoration Experiment: To validate the generalization capability of CPL beyond synthetic data, we conduct a comprehensive evaluation on the real-world WeatherBench dataset [81], as detailed in Table V. Quantitatively, our model attains an average PSNR of 30.35 dB, which is 2.49 dB higher than the PromptIR baseline. The superior LPIPS scores further indicate that these gains translate into perceptible improvements in image quality. As illustrated in Figure 8, baseline methods often struggle with the complexity of real-world degradations. For instance, in the snow removal example, competing methods fail to distinguish between white particle artifacts and the underlying texture, leading to residual noise. In contrast, CPL effectively suppresses weather artifacts while maintaining structural fidelity and color accuracy.

f) Composite Degradation Experiment: To evaluate the capability of handling coexisting degradations, we use the

TABLE IV

QUANTITATIVE COMPARISONS FOR ADVERSE WEATHER REMOVAL. METHODS CAPABLE OF HANDLING MULTIPLE DEGRADATION TASKS ARE LISTED TOGETHER, AND THEIR AVERAGE PERFORMANCE IS PROVIDED AT THE BOTTOM. MISSING VALUES ARE DENOTED BY '—'.

Type	Method	Venue	Snow100K-S [80]		Snow100K-L [80]		Outdoor-Rain [79]		RainDrop [78]		Average	
			PSNR	SSIM	PSNR	SSIM	PSNR	SSIM	PSNR	SSIM	PSNR	SSIM
Task-Specific	SPANet [83]	CVPR'19	29.92	0.8260	23.70	0.7930	—	—	—	—	—	—
	DesnowNet [80]	TIP'18	32.33	0.9500	27.17	0.8983	—	—	—	—	—	—
	HRGAN [79]	CVPR'19	—	—	—	—	21.56	0.8550	—	—	—	—
	MPRNet [66]	CVPR'21	—	—	—	—	28.03	0.9192	—	—	—	—
	AttentiveGAN [78]	CVPR'18	—	—	—	—	—	—	31.59	0.9170	—	—
	IDT [84]	TIP'22	—	—	—	—	—	—	31.87	0.9313	—	—
	NAFNet [36]	ECCV'22	34.79	0.9497	30.06	0.9017	29.59	0.9027	—	—	—	—
	Restormer [21]	CVPR'22	36.01	0.9579	30.36	0.9068	30.03	0.9215	32.18	0.9408	—	—
All-in-One	All-in-One [85]	CVPR'20	—	—	28.33	0.8820	24.71	0.8980	31.12	0.9268	28.05	0.9023
	Transweather [75]	CVPR'22	32.51	0.9341	29.31	0.8879	28.83	0.9000	30.17	0.9157	30.20	0.9094
	WGWSNet [86]	CVPR'22	34.31	0.9460	30.16	0.9007	29.32	0.9207	32.38	0.9378	31.54	0.9263
	WeatherDiff ₆₄ [87]	TPAMI'23	35.83	0.9566	30.09	0.9041	29.64	0.9312	30.71	0.9312	31.57	0.9308
	WeatherDiff ₁₂₈ [87]	TPAMI'23	35.02	0.9516	29.58	0.8941	29.72	0.9216	29.66	0.9225	31.00	0.9225
	AWRCP [88]	ICCV'23	36.92	0.9652	31.92	0.9341	31.39	0.9329	31.93	0.9314	33.04	0.9409
	GridFormer [39]	IJCV'24	37.46	0.9640	31.71	0.9231	31.87	0.9335	32.39	0.9362	33.36	0.9392
	MPerceiver [89]	CVPR'24	36.23	0.9571	31.02	0.9164	31.25	0.9246	33.21	0.9294	32.93	0.9319
	DTPM [90]	CVPR'24	37.01	0.9663	30.92	0.9174	30.99	0.9340	32.72	0.9440	32.91	0.9404
	Histoformer [91]	ECCV'24	37.41	0.9656	<u>32.16</u>	0.9261	<u>32.08</u>	0.9389	<u>33.06</u>	0.9441	33.68	0.9437
	PromptIR [10]	NeurIPS'23	36.88	0.9643	31.34	0.9200	30.80	0.9229	32.20	0.9359	32.80	0.9357
	PromptIR+CPL	2025	37.82	0.9667	32.27	<u>0.9280</u>	32.16	0.9417	32.73	0.9428	33.74	0.9437

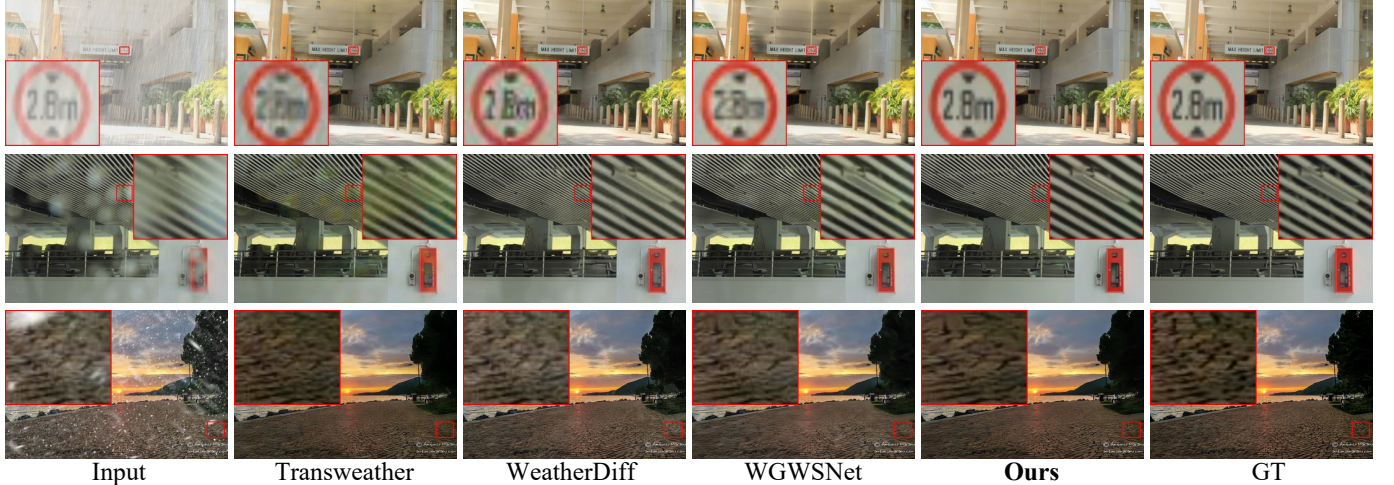


Fig. 7. Visual comparisons on diverse weather degradation datasets. From top to bottom: rain and haze removal (Outdoor-Rain), raindrop removal (RainDrop), and snow removal (Snow100K). CPL removes adverse weather artifacts while preserving fine details.

CDD-11 dataset [82], which contains both single and composite degradations. As shown in Table VI, PromptIR+CPL achieves the highest average PSNR and ranks first in 10 out of 11 categories, with an average of 29.07 dB (0.60 dB higher than OneRestore [82]). These results suggest that CPL improves robustness in composite degradation scenarios. For single degradations, PromptIR+CPL yields large gains over PromptIR, such as 6.69 dB in dehazing and 3.82 dB in desnowing. The advantage is maintained as the degradation complexity increases. For mixed degradations, we observe clear

improvements in challenging combinations such as haze+rain (30.40 dB), and even for third-order composite degradations (e.g., low-light+haze+rain), where the gain over the baseline reaches 1.66 dB. Figure 9 presents visual comparisons for single degradations; for low-light enhancement, CPL provides more balanced illumination while preserving color tones and texture details. Figure 10 shows examples of composite degradations, where CPL reduces multiple artifacts simultaneously and better preserves structural details and color consistency.

TABLE V
QUANTITATIVE COMPARISONS ON REAL-WORLD DEWEATHERING. WE REPORT PSNR, SSIM, AND LPIPS FOR ALL TASKS.

Type	Method	Venue	Dehaze			Derain			Desnow			Average		
			PSNR↑	SSIM↑	LPIPS↓									
General	DehazeFormer [92]	TIP'23	24.12	0.745	0.345	36.05	0.954	0.181	28.88	0.849	0.178	29.68	0.849	0.235
	DCMPNet [93]	CVPR'24	21.18	0.506	0.491	32.04	0.876	0.282	24.81	0.614	0.546	26.01	0.665	0.440
	DRSformer [68]	CVPR'23	19.95	0.694	0.404	33.98	0.943	0.209	28.00	0.836	0.197	27.31	0.824	0.270
	NeRD-Rain [94]	CVPR'24	21.52	0.718	0.386	35.74	0.950	0.182	28.87	0.851	0.182	28.71	0.840	0.250
	SnowFormer [95]	arXiv'22	22.71	0.736	0.305	35.18	0.951	0.155	29.30	0.868	0.143	29.06	0.852	0.201
	MPRNet [66]	CVPR'21	23.27	0.739	0.355	36.14	0.954	0.171	29.18	0.860	0.177	29.53	0.851	0.234
	Restormer [21]	CVPR'22	19.30	0.687	0.412	34.49	0.945	0.197	27.95	0.836	0.197	27.25	0.823	0.269
All-in-One	AirNet	CVPR'22	20.94	0.705	0.383	33.59	0.942	0.224	22.06	0.780	0.291	25.53	0.809	0.299
	TransWeather [75]	CVPR'22	19.79	0.680	0.397	29.34	0.903	0.294	24.96	0.796	0.231	24.70	0.793	0.307
	WGWS-Net [86]	CVPR'23	13.79	0.603	0.535	37.08	0.961	0.117	20.81	0.780	0.248	23.89	0.781	0.300
	DiffUIR [96]	CVPR'24	22.74	0.744	0.355	35.93	0.955	0.172	29.50	0.870	0.162	29.39	0.856	0.230
	MWFFormer [97]	TIP'24	<u>24.42</u>	<u>0.746</u>	0.284	35.15	0.951	<u>0.153</u>	<u>29.98</u>	0.872	0.133	<u>29.85</u>	<u>0.856</u>	0.190
	Histoformer [91]	ECCV'24	17.69	0.669	0.437	30.70	0.916	0.279	25.39	0.808	0.225	24.59	0.798	0.314
	AdaIR [11]	ICLR'25	23.08	0.731	0.351	34.87	0.946	0.192	28.44	0.837	0.179	28.80	0.838	0.240
	PromptIR [10]	NeurIPS'23	21.11	0.713	0.375	34.54	0.944	0.198	27.93	0.836	0.195	27.86	0.831	0.256
	PromptIR+CPL	2025	24.48	0.747	0.339	<u>36.57</u>	<u>0.958</u>	0.168	30.02	0.863	0.172	30.35	0.856	0.226

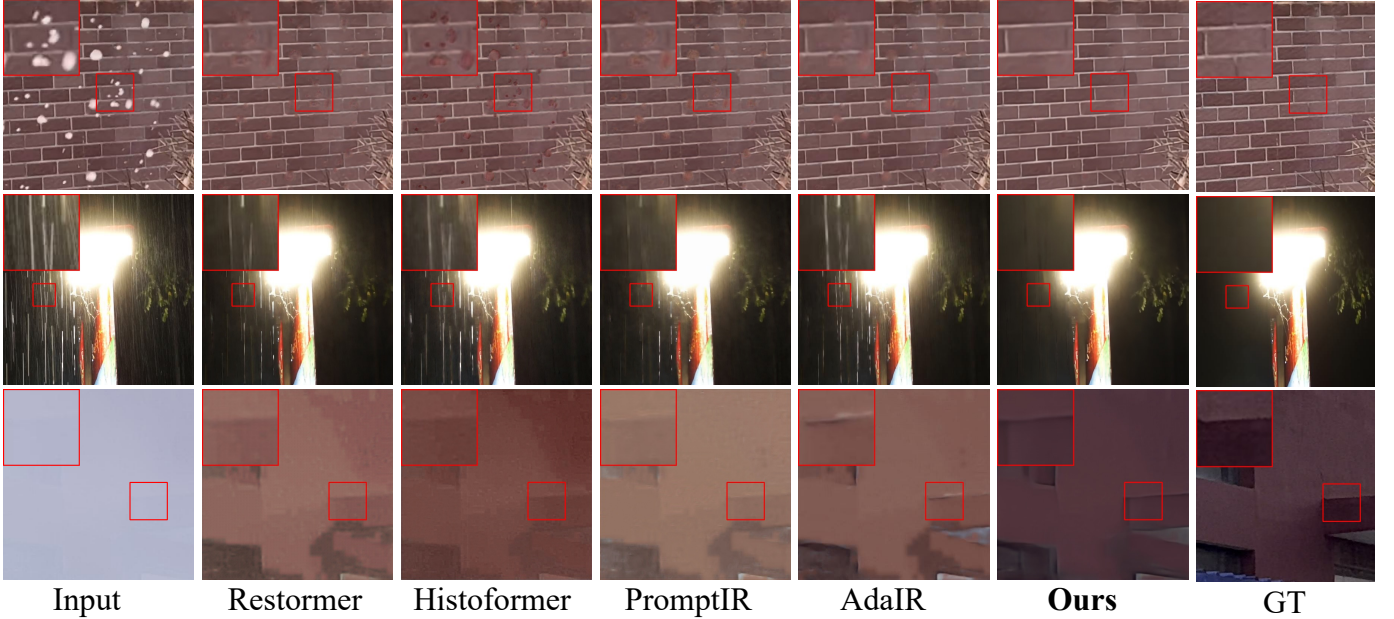


Fig. 8. Visual comparisons on real-world adverse weather scenes from WeatherBench [81]. From top to bottom: snow, night rain, and haze. CPL improves visibility and texture details compared with baseline methods.

D. Ablation Studies

In this section, we conduct a series of detailed ablation experiments to dissect the key components and hyperparameters of our CPL framework. We analyze the impact of the sparsity level by varying the number of activated prompts, k , in the top- k gating mechanism. As shown in Tables VII

and VIII, the optimal choice of k reveals a trade-off between specialization and collaboration. On the three-task benchmark, where degradations share certain statistical similarities (e.g., rain streaks and noise), setting $k = 2$ yields the highest PSNR (32.54 dB). This suggests that allowing a slight relaxation of sparsity, enabling two complementary prompts to collaborate, provides flexibility for handling overlapping degradation patterns. However, increasing k further to three results in a performance drop, confirming that excessive prompt activation reintroduces the representation redundancy that SPM is designed to mitigate. Conversely, on the more

a) *Effect of Prompt Sparsity in SPM*: To rigorously isolate the contribution of the SPM, we conduct this ablation without the proposed CPR. We investigate the impact of the sparsity level by varying the number of activated prompts, k , in the top- k gating mechanism. As shown in Tables VII

TABLE VI

QUANTITATIVE EVALUATION ON THE COMPOSITE DEGRADATION BENCHMARK FOLLOWING [82]. SINGLE AND MULTIPLE COMPOSITE DEGRADATIONS ARE EVALUATED ON THE CDD-11 DATASET.

Method	Venue	l	h	r	s	l+h	l+r	l+s	h+r	h+s	l+h+r	l+h+s	Avg.
AirNet [9]	CVPR'22	24.83	24.21	26.55	26.79	23.23	22.82	23.29	22.21	23.29	21.80	22.24	23.75
TransWeather [75]	CVPR'22	23.39	23.95	26.69	25.74	22.24	22.62	21.80	23.10	22.34	21.55	21.01	23.13
WeatherDiff [87]	TPAMI'23	23.58	21.99	24.85	24.80	21.83	22.69	22.12	21.25	21.99	21.23	21.04	22.49
WGWSNet [86]	CVPR'23	24.39	27.90	33.15	34.43	24.27	25.06	24.60	27.23	27.65	23.90	23.97	26.96
InstructIR [50]	ECCV'24	<u>26.70</u>	32.61	<u>33.51</u>	34.45	24.36	25.41	<u>25.63</u>	28.80	29.64	24.84	24.32	28.21
OneRestore [82]	ECCV'24	26.55	<u>32.71</u>	33.48	<u>34.50</u>	<u>26.15</u>	<u>25.83</u>	25.56	<u>30.27</u>	30.46	<u>25.18</u>	<u>25.28</u>	<u>28.47</u>
PromptIR [10]	NeurIPS'23	26.32	26.10	31.56	31.53	24.49	25.05	24.51	24.54	23.70	23.74	23.33	25.90
PromptIR+CPL	2025	27.35	32.79	34.60	35.35	26.18	26.32	26.10	30.40	29.95	25.40	25.35	29.07

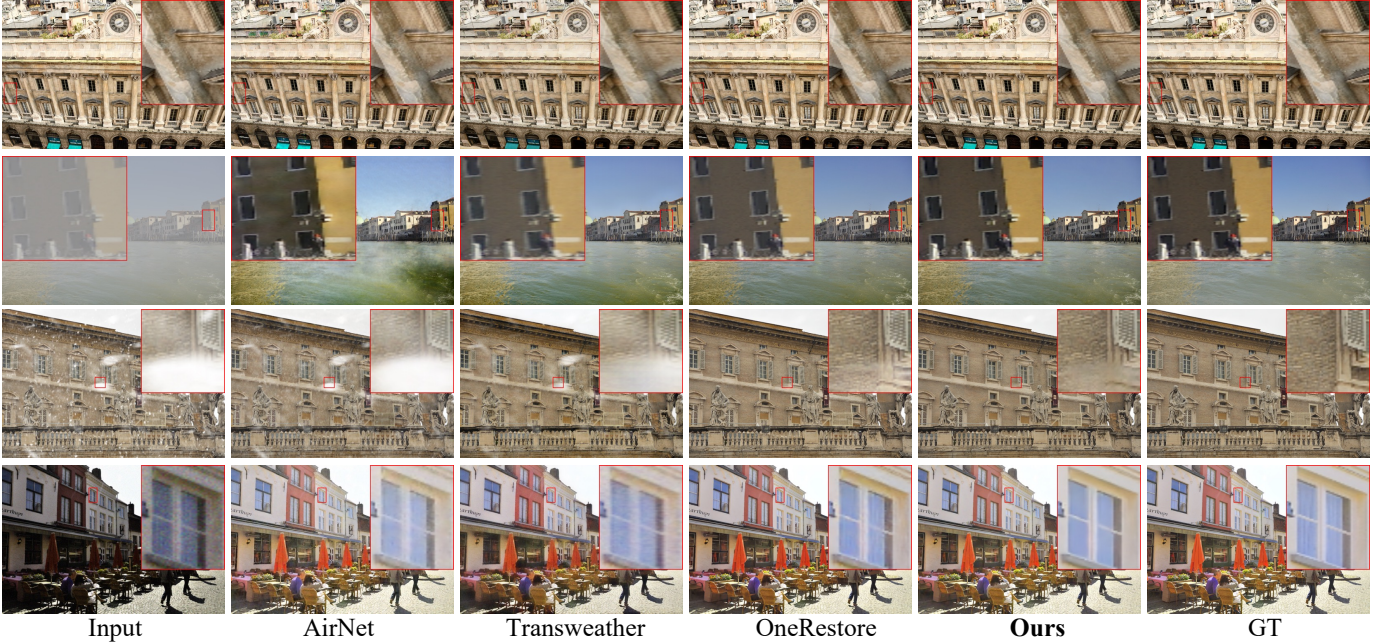


Fig. 9. Visual comparisons on single-degradation cases from the composite degradation dataset. From top to bottom: deraining, dehazing, desnowing, and low-light enhancement. CPL removes degradations while maintaining scene structures and natural color appearance.

diverse five-task benchmark, which involves distinct physical mechanisms (e.g., global illumination in low-light vs. local motion blur), resulting in $k = 1$ proves optimal. This constraint compels the model to rely on a single, highly specialized prompt representation, effectively preventing interference from irrelevant task priors.

Based on these findings, we adopt $k = 1$ as the default setting for all main experiments to prioritize clear task boundaries in complex scenarios. It is worth noting that the results in this ablation are lower than the final performance reported in Tables I and II. This gap showcases the significant contribution of CPR, which further boosts performance by explicitly enforcing functional alignment between the selected prompt and the restoration objective.

b) Prompt Selection Patterns: To further examine the effect of the proposed modules, we visualize prompt selection patterns during inference on the Rain100L test set in Figure 11. The baseline PromptIR model (Figure 11(a)) shows a diffuse selection distribution, where activations are spread across multiple prompt indices for most samples. This

observation is consistent with our entropy analysis and suggests that adaptive prompts without additional constraints tend to develop redundant and overlapping representations. After introducing the SPM (Figure 11(b)), the selection becomes more concentrated, with most samples relying on a small subset of prompts, indicating more task-specific usage of prompt capacity. When CPR is further added (Figure 11(c)), the selection pattern becomes even more consistent across samples. This progression from (a) to (c) is in line with our design goal: combining sparse selection with contrastive regularization encourages prompts that are more specialized and better aligned with the restoration tasks.

c) Prompt Scalability Analysis: To evaluate how effectively our sparse prompt design scales compared with dense alternatives, we increase the number of available prompts from 5 to 15 for both PromptIR and CPL on the CDD-11 benchmark. Two observations emerge from Table IX. First, the dense ensembling strategy in PromptIR exhibits clear diminishing returns: tripling the number of prompts and parameters yields only a marginal average PSNR gain of +0.20 dB (from



Fig. 10. Visual comparisons on composite degradations from the composite degradation dataset: low-light+haze+rain (top row) and low-light+haze+snow (bottom row). CPL simultaneously reduces multiple degradations and preserves structural details and color fidelity.

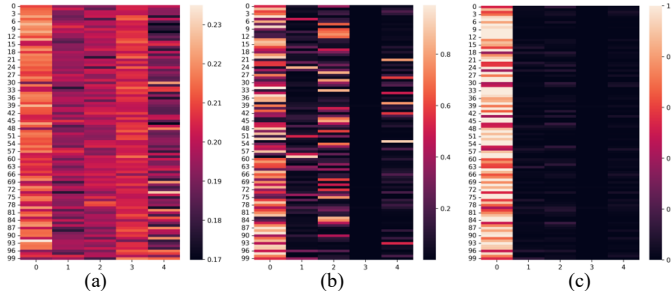


Fig. 11. Visualization of prompt selection patterns across 100 test images from the Rain100L dataset, where the x-axis represents prompt indices and the y-axis represents sample indices. (a) Baseline PromptIR with adaptive prompts. (b) CPL with the SPM. (c) CPL with both SPM and CPR.

25.90 dB to 26.10 dB), together with an increase in FLOPs. This suggests that simply adding more dense prompts largely amplifies existing redundancy rather than providing genuinely new task-specialized capacity. In contrast, CPL shows a more favorable scaling behavior. Under the same increase in prompt capacity, our model improves by +0.78 dB (from 29.07 dB to 29.85 dB), which is almost four times the gain observed for PromptIR, while keeping the inference FLOPs nearly constant due to the top- k sparse routing in SPM. This pattern is consistent with our hypothesis that unconstrained dense ensembling tends to suffer from representation redundancy and limited capacity utilization, whereas enforcing sparsity at the prompt level allows the model to better exploit a larger and more diverse prompt pool for performance scaling.

TABLE VII

ABALATION STUDY ON THE VALUE OF k IN OUR SPM ON THE THREE-TASK BENCHMARK.

Method	Denoising on BSD68			Average
	Dehazing on SOTS	Deraining on Rain100L	$\sigma=15$	
Baseline	30.58 / 0.974	36.37 / 0.972	33.98 / 0.933	32.06 / 0.913
Ours ($k = 1$)	30.60 / 0.975	38.30 / 0.983	34.00 / 0.930	32.48 / 0.913
Ours ($k = 2$)	30.66 / 0.977	38.45 / 0.984	34.05 / 0.931	32.54 / 0.914
Ours ($k = 3$)	30.41 / 0.972	37.57 / 0.979	33.93 / 0.928	32.23 / 0.911

d) Computational Efficiency Analysis: The same experiment also highlights the computational efficiency of our framework. As detailed in Table IX, even in a parameter-matched setting with 5 prompts, our SPM is inherently more efficient, reducing FLOPs by 5% compared to PromptIR while delivering significantly higher accuracy. More critically,

TABLE VIII
ABLATION STUDY ON THE VALUE OF k IN OUR SPM ON THE FIVE-TASK BENCHMARK.

Method	Denoising CBSD68	Dehazing SOTS	Deraining Rain100L	Deblurring GoPro	Low-light LOL	Average
Baseline	31.47 / 0.886	26.54 / 0.949	36.37 / 0.970	28.71 / 0.881	22.68 / 0.832	29.15 / 0.904
Ours ($k = 1$)	31.35 / 0.886	29.67 / 0.963	37.47 / 0.974	28.67 / 0.881	23.12 / 0.844	30.06 / 0.908
Ours ($k = 2$)	31.29 / 0.885	28.83 / 0.959	36.91 / 0.972	28.44 / 0.885	22.97 / 0.838	29.68 / 0.906
Ours ($k = 3$)	31.28 / 0.885	28.37 / 0.952	36.75 / 0.972	28.42 / 0.885	22.92 / 0.837	29.54 / 0.905

the efficiency gap widens as the model scales. Because the inference cost of SPM depends only on the number of activated experts ($k = 1$), our model's FLOPs remain constant at 43.18 GFLOPs regardless of the total number of prompts available. Conversely, PromptIR's computational cost increases linearly with the number of prompts. Consequently, our 15-prompt model is better than its 15-prompt PromptIR counterpart and 14.2% more computationally efficient. This demonstrates that our CPL framework achieves superior performance and scalability without the typical trade-off in computational cost, offering a more practical solution for real-world deployment.

e) Cross-Architecture Evaluation: To validate the plug-and-play nature and architecture-agnostic benefits of our CPL framework, we integrated it into four diverse, high-performing restoration backbones: NAFNet and FSNet (CNN-based), DRSformer (Transformer-based), and MambaIR (state-space model). We retrained each model on the five-task benchmark, and the results are presented in Table X. Across all backbones, CPL yields consistent improvements in average PSNR, with gains ranging from +1.01 dB for MambaIR to +1.15 dB for FSNet. The presence of similar gains across architectures with markedly different inductive biases suggests that CPL acts as a generally applicable enhancement module, rather than a mechanism tailored to a specific network design.

f) Sensitivity Analysis on the CPR Loss Weight: We analyze the model's sensitivity to the hyperparameter α in Eq. (8), which balances the contrastive prompt regularization \mathcal{L}_{cpr} against the primary reconstruction loss. We trained models on both the three-task and five-task benchmarks while varying α across a wide range from 0.001 to 0.3. As shown in Table XI, our method exhibits strong robustness to this choice. Performance remains stable across the range of 10^{-3} to 10^{-2} , with optimal results achieved at $\alpha = 0.003$ for the three-task setting and $\alpha = 0.01$ for the five-task setting. This indicates that a small weighting for the CPR term is sufficient to guide the model towards functional alignment

TABLE IX

EFFICIENCY AND SCALABILITY COMPARISON ON THE CDD-11 BENCHMARK. OUR SPARSE PROMPT DESIGN IS MORE EFFICIENT AND SCALES FAR MORE EFFECTIVELY THAN THE DENSE APPROACH OF PROMPTIR.

Method	Prompts	Params. (M)	FLOPs (G)	l	h	r	s	l+h	l+r	l+s	h+r	h+s	l+h+r	l+h+s	Avg.
PromptIR	5	35.38	45.55	26.32	26.10	31.56	31.53	24.49	25.05	24.51	24.54	23.70	23.74	23.33	25.90
	10	37.76	47.93	26.41	26.19	31.65	31.60	24.62	25.15	24.60	24.68	23.81	23.85	23.45	26.05
	15	40.14	50.31	26.45	26.23	31.69	31.62	24.68	25.20	24.63	24.75	23.88	23.90	23.51	26.10
Ours	5	35.38	43.18	27.35	32.79	34.60	35.35	26.18	26.32	26.10	30.40	29.95	25.40	25.35	29.07
	10	37.76	43.18	27.48	34.91	35.00	35.96	26.70	26.55	26.38	31.52	31.49	25.79	25.83	29.60
	15	40.14	43.18	27.56	35.85	35.23	36.25	26.95	26.65	26.54	32.14	32.07	26.07	26.01	29.85

TABLE X

PLUG-AND-PLAY EVALUATION OF CPL INTEGRATED INTO DIFFERENT RESTORATION BACKBONES ON THE FIVE-TASK BENCHMARK.

Method	Venue	Denoising CBSD68	Dehazing SOTS	Deraining Rain100L	Deblurring GoPro	Low-light LOL	Average
NAFNet [36] NAFNet+CPL	ECCV'22	31.02 / 0.883	25.23 / 0.939	35.56 / 0.967	26.53 / 0.808	20.49 / 0.809	27.76 / 0.881
		31.15 / 0.883	28.18 / 0.951	37.47 / 0.973	28.78 / 0.829	22.27 / 0.827	29.57 / 0.893
DRSformer [68] DRSformer+CPL	CVPR'23	30.97 / 0.881	24.66 / 0.931	33.45 / 0.953	25.56 / 0.780	21.77 / 0.821	27.28 / 0.873
		31.18 / 0.881	27.19 / 0.945	35.20 / 0.961	27.61 / 0.801	22.42 / 0.833	28.72 / 0.884
FSNet [67] FSNet+CPL	TPAMI'23	31.33 / 0.883	25.53 / 0.943	36.07 / 0.968	28.32 / 0.869	22.29 / 0.829	28.71 / 0.898
		31.44 / 0.884	28.71 / 0.954	37.82 / 0.975	28.73 / 0.877	22.62 / 0.834	29.86 / 0.905
MambaIR [40] MambaIR+CPL	ECCV'24	31.41 / 0.884	25.81 / 0.944	36.55 / 0.971	28.61 / 0.875	22.49 / 0.832	28.97 / 0.901
		31.50 / 0.886	28.84 / 0.958	37.94 / 0.976	28.83 / 0.884	22.79 / 0.836	29.98 / 0.908

without disrupting the primary restoration objective. We select $\alpha = 0.01$ as a unified default for all experiments, as it provides near-optimal performance across benchmarks without requiring task-specific tuning. This stability underscores the reliability and ease of implementation of our CPR strategy.

TABLE XI

SENSITIVITY ANALYSIS OF THE CPR LOSS WEIGHT α . RESULTS ARE REPORTED ON BOTH THREE-TASK AND FIVE-TASK BENCHMARKS.

Task	$\alpha = 0.001$	$\alpha = 0.003$	$\alpha = 0.01$	$\alpha = 0.03$	$\alpha = 0.1$	$\alpha = 0.3$
Three-Task Benchmark	32.78	32.81	32.78	32.75	32.75	32.69
Five-Task Benchmark	30.42	30.47	30.55	30.53	30.49	30.38

g) Effect of the Number of Negative Samples: We investigate the impact of the number of negative samples on restoration performance, as detailed in Table XII. The results reveal a clear relationship between the diversity of negative constraints and model efficacy. Introducing a single negative sample yields a substantial gain of 0.52 dB over the baseline, validating our premise that explicitly penalizing functional misalignment significantly enhances task specificity. As we increase the number to 4, the performance improves and peaks at 32.78 dB. This trend suggests that exposing the model to a wider variety of “incorrect” prompts helps establish sharper functional boundaries, compelling the network to adhere more strictly to the guidance of the target prompt. However, further increasing the number to 8 results in a slight saturation (32.75 dB), indicating diminishing returns and a potential dilution of the primary reconstruction gradient by redundant repulsive signals. We adopt 4 negative samples as the optimal trade-off between regularization strength and training stability.

TABLE XII

ABLATION STUDY ON THE NUMBER OF NEGATIVE SAMPLES IN CPR. PERFORMANCE IS EVALUATED ON THE THREE-TASK BENCHMARK.

Method	PSNR (dB)
Baseline (PromptIR)	32.06
CPR w/ 1 Negative Sample	32.58
CPR w/ 2 Negative Samples	32.66
CPR w/ 4 Negative Samples	32.78
CPR w/ 8 Negative Samples	32.75

E. Limitations and Future Work

While our CPL framework demonstrates notable advancements in mitigating prompt redundancy and enhancing functional alignment, we acknowledge certain limitations. The main limitation lies in our CPR strategy. CPR currently constructs negative samples by treating all mismatched prompt-task pairings as equally negative. For instance, when restoring a low-light image, a prompt for a visually similar task like dehazing is penalized with the same repulsive force as a prompt for a highly dissimilar task like denoising. This uniform negative sampling strategy, while effective at enforcing task specificity, oversimplifies the complex web of inter-task relationships and does not explicitly leverage the semantic similarities and differences between various degradation types.

This limitation opens up several promising avenues for future research. A direct extension would be to develop more sophisticated negative sampling strategies for CPR. Instead of uniform sampling, one could implement a semantic-aware weighting scheme, where the repulsive force is modulated by the similarity between the ground-truth task and the negative prompt’s task. This could allow the model to learn a more nuanced and structured prompt space. An even more ambitious direction would be to move beyond the binary contrastive paradigm altogether. Inspired by recent advance-

ments in large model alignment, one could formulate the regularization as a preference learning problem. Rather than a simple positive/negative distinction, the model could be trained to learn a fine-grained preference for “better” restorations over “worse” ones, even when both are generated by sub-optimal prompts. Such a paradigm, conceptually related to Reinforcement Learning from Human Feedback (RLHF), could help the model learn a more detailed understanding of image quality and task relationships, further enhancing its generalization capabilities in complex, real-world scenarios.

V. CONCLUSION

In this paper, we address the inherent challenges of representation redundancy and functional misalignment that hinder existing AiOIR frameworks. We propose a Contrastive Prompt Learning (CPL) framework that resolves this tension through two synergistic conceptual shifts in prompt design and regularization. First, the Sparse Prompt Module (SPM) tackles representation redundancy by leveraging principled sparsity to enhance the intrinsic quality and expressive power of each individual prompt. Complementing this, the Contrastive Prompt Regularization (CPR) mechanism addresses functional misalignment. It introduces a novel paradigm of functional regularization via a model-prompt decoupling strategy, which optimizes prompts for their behavioral alignment and reconstruction quality, rather than for abstract classification. Comprehensive experiments across a wide array of benchmarks validate the superiority of our approach. The consistent and significant performance improvements demonstrate that our synergistic design effectively addresses the core limitations of current prompt-based models. Beyond the immediate performance gains, our work suggests that an effective path to robust AiOIR is to co-design the intrinsic quality of prompts together with their functional alignment to the restoration model.

REFERENCES

- [1] M. Banham and A. Katsaggelos, “Digital image restoration,” *IEEE Signal Process. Maga.*, vol. 14, no. 2, pp. 24–41, 1997.
- [2] J. Su, B. Xu, and H. Yin, “A survey of deep learning approaches to image restoration,” *Neurocomput.*, vol. 487, pp. 46–65, 2022-05.
- [3] M. Elad, B. Kawar, and G. Vaksman, “Image denoising: The deep learning revolution and beyond - A survey paper,” *SIAM J. Imaging Sci.*, vol. 16, no. 3, pp. 1594–1654, 2023.
- [4] K. Zhang, W. Ren, W. Luo, W. Lai, B. Stenger, M. Yang, and H. Li, “Deep image deblurring: A survey,” *Int. J. Comput. Vis.*, vol. 130, no. 9, pp. 2103–2130, 2022.
- [5] X. Chen, J. Pan, J. Dong, and J. Tang, “Towards unified deep image deraining: A survey and a new benchmark,” *IEEE Trans. Pattern Anal. Mach. Intell.*, vol. 47, no. 7, pp. 5414–5433, 2025.
- [6] J. Gui, X. Cong, Y. Cao, W. Ren, J. Zhang, J. Zhang, J. Cao, and D. Tao, “A comprehensive survey and taxonomy on single image dehazing based on deep learning,” *ACM Comput. Surv.*, vol. 55, no. 13s, pp. 279:1–279:37, 2023.
- [7] C. Li, C. Guo, L. Han, J. Jiang, M. Cheng, J. Gu, and C. C. Loy, “Low-light image and video enhancement using deep learning: A survey,” *IEEE Trans. Pattern Anal. Mach. Intell.*, vol. 44, no. 12, pp. 9396–9416, 2022.
- [8] J. Jiang, Z. Zuo, G. Wu, K. Jiang, and X. Liu, “A survey on all-in-one image restoration: Taxonomy, evaluation and future trends,” *IEEE Trans. Pattern Anal. Mach. Intell.*, vol. 47, no. 12, pp. 11 892–11 911, 2025.
- [9] B. Li, X. Liu, P. Hu, Z. Wu, J. Lv, and X. Peng, “All-in-one image restoration for unknown corruption,” in *IEEE Conf. Comput. Vis. Pattern Recog.*, 2022, pp. 17 431–17 441.
- [10] V. Potlapalli, S. W. Zamir, S. H. Khan, and F. S. Khan, “PromptIR: Prompting for all-in-one image restoration,” in *Adv. Neural Inform. Process. Syst.*, 2023.
- [11] Y. Cui, S. W. Zamir, S. H. Khan, A. Knoll, M. Shah, and F. S. Khan, “AdaIR: Adaptive all-in-one image restoration via frequency mining and modulation,” in *Int. Conf. Learn. Represent.*, 2025.
- [12] X. Kong, C. Dong, and L. Zhang, “Towards effective multiple-in-one image restoration: A sequential and prompt learning strategy,” *CoRR*, vol. abs/2401.03379, 2024.
- [13] Z. Luo, F. K. Gustafsson, Z. Zhao, J. Sjölund, and T. B. Schön, “Controlling vision-language models for multi-task image restoration,” in *Int. Conf. Learn. Represent.*, 2024.
- [14] J. Hu, L. Jin, Z. Yao, and Y. Lu, “Universal image restoration pre-training via degradation classification,” in *Int. Conf. Learn. Represent.*, 2025.
- [15] G. Kim and J. Kwon, “Deep illumination-aware dehazing with low-light and detail enhancement,” *IEEE Trans. Intell. Transport. Syst.*, vol. 23, no. 3, pp. 2494–2508, 2022.
- [16] Q. Zheng, B. Shi, X. Jiang, L.-Y. Duan, and A. C. Kot, “Denoising adversarial networks for rain removal and reflection removal,” in *IEEE Int. Conf. Image Process.*, 2019, pp. 2766–2770.
- [17] Z. Wan, B. Zhang, D. Chen, P. Zhang, F. Wen, and J. Liao, “Old photo restoration via deep latent space translation,” *IEEE Trans. Pattern Anal. Mach. Intell.*, vol. 45, no. 2, pp. 2071–2087, 2022.
- [18] K. Zhang, Y. Li, J. Liang, J. Cao, Y. Zhang, H. Tang, D. Fan, R. Timofte, and L. V. Gool, “Practical blind image denoising via swin-conv-unet and data synthesis,” *Mach. Intell. Res.*, vol. 20, no. 6, pp. 822–836, 2023.
- [19] J. Pan, D. Sun, H. Pfister, and M.-H. Yang, “Deblurring images via dark channel prior,” *IEEE Trans. Pattern Anal. Mach. Intell.*, vol. 40, no. 10, pp. 2315–2328, 2018.
- [20] Y. Cui, Y. Tao, W. Ren, and A. Knoll, “Dual-domain attention for image deblurring,” in *AAAI Conf. Artif. Intell.*, 2023, pp. 479–487.
- [21] S. W. Zamir, A. Arora, S. Khan, M. Hayat, F. S. Khan, and M.-H. Yang, “Restorer: Efficient transformer for high-resolution image restoration,” in *IEEE Conf. Comput. Vis. Pattern Recog.*, 2022, pp. 5718–5729.
- [22] Y. Quan, Z. Wu, R. Xu, and H. Ji, “Deep single image defocus deblurring via gaussian kernel mixture learning,” *IEEE Trans. Pattern Anal. Mach. Intell.*, vol. 46, no. 12, pp. 11 361–11 377, 2024.
- [23] X. Qin, Z. Wang, Y. Bai, X. Xie, and H. Jia, “FFA-Net: Feature fusion attention network for single image dehazing,” in *AAAI Conf. Artif. Intell.*, 2020, pp. 11 908–11 915.
- [24] Y. Cui, W. Ren, X. Cao, and A. Knoll, “Revitalizing convolutional network for image restoration,” *IEEE Transactions on Pattern Analysis and Machine Intelligence*, vol. 46, no. 12, pp. 9423–9438, 2024.
- [25] Y. Feng, L. Ma, X. Meng, F. Zhou, R. Liu, and Z. Su, “Advancing real-world image dehazing: Perspective, modules, and training,” *IEEE Trans. Pattern Anal. Mach. Intell.*, vol. 46, no. 12, pp. 9303–9320, 2024.
- [26] Y. Cui, Q. Wang, C. Li, W. Ren, and A. Knoll, “EENet: An effective and efficient network for single image dehazing,” *Pattern Recognit.*, vol. 158, p. 111074, 2025.
- [27] K. Jiang, Z. Wang, P. Yi, C. Chen, B. Huang, Y. Luo, J. Ma, and J. Jiang, “Multi-scale progressive fusion network for single image deraining,” in *IEEE Conf. Comput. Vis. Pattern Recog.*, 2020, pp. 8346–8355.
- [28] K. Jiang, Z. Wang, P. Yi, C. Chen, Z. Wang, X. Wang, J. Jiang, and C.-W. Lin, “Rain-free and residue hand-in-hand: A progressive coupled network for real-time image deraining,” *IEEE Trans. Image Process.*, vol. 30, pp. 7404–7418, 2021.
- [29] H. Huang, M. Luo, and R. He, “Memory uncertainty learning for real-world single image deraining,” *IEEE Trans. Pattern Anal. Mach. Intell.*, vol. 45, no. 3, pp. 3446–3460, 2023.
- [30] W.-Y. Hsu and W.-C. Chang, “Wavelet approximation-aware residual network for single image deraining,” *IEEE Trans. Pattern Anal. Mach. Intell.*, vol. 45, no. 12, pp. 15 979–15 995, 2023.
- [31] K. Jiang, J. Jiang, Z. Wang, Z. Geng, and X. Liu, “DAWN+: Wavelet-based image deraining meets direction-aware attention and mutual representation,” *IEEE Trans. Neural Netw. Learn. Syst.*, vol. 36, no. 10, pp. 18 244–18 258, 2025.
- [32] Y. Cai, H. Bian, J. Lin, H. Wang, R. Timofte, and Y. Zhang, “Retinex-former: One-stage retinex-based transformer for low-light image enhancement,” in *Int. Conf. Comput. Vis.*, 2023, pp. 12 470–12 479.
- [33] Y. Dai, C. Li, S. Zhou, R. Feng, Y. Luo, and C. C. Loy, “Flare7k++: Mixing synthetic and real datasets for nighttime flare removal and beyond,” *IEEE Trans. Pattern Anal. Mach. Intell.*, vol. 46, no. 11, pp. 7041–7055, 2024.
- [34] Q. Wang, Y. Cui, Y. Li, Y. Ruan, B. Zhu, and W. Ren, “RFFNet: Towards robust and flexible fusion for low-light image denoising,” in *ACM Int. Conf. Multimedia*, 2024, pp. 836–845.

[35] Z. Zhang, S. Zhao, X. Jin, M. Xu, Y. Yang, S. Yan, and M. Wang, “Noise self-regression: A new learning paradigm to enhance low-light images without task-related data,” *IEEE Trans. Pattern Anal. Mach. Intell.*, vol. 47, no. 2, pp. 1073–1088, 2025.

[36] L. Chen, X. Chu, X. Zhang, and J. Sun, “Simple baselines for image restoration,” in *Eur. Conf. Comput. Vis.*, vol. 13667, 2022, pp. 17–33.

[37] H. Chen, Y. Wang, T. Guo, C. Xu, Y. Deng, Z. Liu, S. Ma, C. Xu, C. Xu, and W. Gao, “Pre-trained image processing transformer,” in *IEEE Conf. Comput. Vis. Pattern Recog.*, 2021, pp. 12299–12310.

[38] Z. Wang, X. Cun, J. Bao, W. Zhou, J. Liu, and H. Li, “Uformer: A general u-shaped transformer for image restoration,” in *IEEE Conf. Comput. Vis. Pattern Recog.*, 2022, pp. 17662–17672.

[39] T. Wang, K. Zhang, Z. Shao, W. Luo, B. Stenger, T. Lu, T. Kim, W. Liu, and H. Li, “GridFormer: Residual dense transformer with grid structure for image restoration in adverse weather conditions,” *Int. J. Comput. Vis.*, vol. 132, no. 10, pp. 4541–4563, 2024.

[40] H. Guo, J. Li, T. Dai, Z. Ouyang, X. Ren, and S. Xia, “Mambair: A simple baseline for image restoration with state-space model,” in *Eur. Conf. Comput. Vis.*, vol. 15076, 2024, pp. 222–241.

[41] Y. Cui, M. Liu, W. Ren, and A. Knoll, “Hybrid frequency modulation network for image restoration,” in *Int. Jt. Conf. Artif. Intell.*, 2024, pp. 722–730.

[42] B. Li, H. Zhao, W. Wang, P. Hu, Y. Gou, and X. Peng, “MaIR: A locality- and continuity-preserving mamba for image restoration,” in *IEEE Conf. Comput. Vis. Pattern Recog.*, 2025.

[43] O. Belhassen, Y. Romano, D. Freedman, E. Rivlin, and M. Elad, “Principal uncertainty quantification with spatial correlation for image restoration problems,” *IEEE Trans. Pattern Anal. Mach. Intell.*, vol. 46, no. 5, pp. 3321–3333, 2024.

[44] Z. Yue and C. C. Loy, “Difface: Blind face restoration with diffused error contraction,” *IEEE Trans. Pattern Anal. Mach. Intell.*, vol. 46, no. 12, pp. 9991–10004, 2024.

[45] M. Li, Y. Fu, T. Zhang, J. Liu, D. Dou, C. Yan, and Y. Zhang, “Latent diffusion enhanced rectangle transformer for hyperspectral image restoration,” *IEEE Trans. Pattern Anal. Mach. Intell.*, vol. 47, no. 1, pp. 549–564, 2025.

[46] Z. Yue, J. Wang, and C. C. Loy, “Efficient diffusion model for image restoration by residual shifting,” *IEEE Trans. Pattern Anal. Mach. Intell.*, vol. 47, no. 1, pp. 116–130, 2025.

[47] J. Zhang, J. Huang, M. Yao, Z. Yang, H. Yu, M. Zhou, and F. Zhao, “Ingredient-oriented multi-degradation learning for image restoration,” in *IEEE Conf. Comput. Vis. Pattern Recog.*, 2023, pp. 5825–5835.

[48] A. Radford, J. W. Kim, C. Hallacy, A. Ramesh, G. Goh, S. Agarwal, G. Sastry, A. Askell, P. Mishkin, J. Clark, G. Krueger, and I. Sutskever, “Learning transferable visual models from natural language supervision,” in *Int. Conf. Mach. Learn.*, vol. 139, 2021, pp. 8748–8763.

[49] J. Lin, Z. Zhang, Y. Wei, D. Ren, D. Jiang, Q. Tian, and W. Zuo, “Improving image restoration through removing degradations in textual representations,” in *IEEE Conf. Comput. Vis. Pattern Recog.*, 2024, pp. 2866–2878.

[50] M. V. Conde, G. Geigle, and R. Timofte, “High-quality image restoration following human instructions,” in *Eur. Conf. Comput. Vis.*, 2024, pp. 1–12.

[51] G. Wu, J. Jiang, K. Jiang, and X. Liu, “Harmony in diversity: Improving all-in-one image restoration via multi-task collaboration,” in *ACM Int. Conf. Multimedia*, 2024, pp. 6015–6023.

[52] G. Wu, J. Jiang, Y. Wang, K. Jiang, and X. Liu, “Debiased all-in-one image restoration with task uncertainty regularization,” in *AAAI Conf. Artif. Intell.*, 2025, pp. 8386–8394.

[53] C. Qin, R. Wu, Z. Liu, X. Lin, C. Guo, H. H. Park, and C. Li, “Restore anything with masks: Leveraging mask image modeling for blind all-in-one image restoration,” in *Eur. Conf. Comput. Vis.*, vol. 15103, 2024, pp. 364–380.

[54] E. Zamfir, Z. Wu, N. Mehta, Y. Tan, D. P. Paudel, Y. Zhang, and R. Timofte, “Complexity experts are task-discriminative learners for any image restoration,” in *IEEE Conf. Comput. Vis. Pattern Recog.*, 2025, pp. 12753–12763.

[55] J. Gui, T. Chen, J. Zhang, Q. Cao, Z. Sun, H. Luo, and D. Tao, “A Survey on Self-Supervised Learning: Algorithms, Applications, and Future Trends,” *IEEE Trans. Pattern Anal. Mach. Intell.*, vol. 46, no. 12, pp. 9052–9071, 2024.

[56] H. Wu, Y. Qu, S. Lin, J. Zhou, R. Qiao, Z. Zhang, Y. Xie, and L. Ma, “Contrastive learning for compact single image dehazing,” in *IEEE Conf. Comput. Vis. Pattern Recog.*, 2021, pp. 10551–10560.

[57] Y. Zheng, J. Zhan, S. He, J. Dong, and Y. Du, “Curricular contrastive regularization for physics-aware single image dehazing,” in *IEEE Conf. Comput. Vis. Pattern Recog.*, 2023, pp. 5785–5794.

[58] G. Wu, J. Jiang, and X. Liu, “A practical contrastive learning framework for single-image super-resolution,” *IEEE Trans. Neural Netw. Learn. Syst.*, vol. 35, no. 11, pp. 15834–15845, 2024.

[59] W. Ran, P. Ma, Z. He, H. Ren, and H. Lu, “Harnessing joint rain-/detail-aware representations to eliminate intricate rains,” in *Int. Conf. Learn. Represent.*, 2024.

[60] Y. Chang, Y. Guo, Y. Ye, C. Yu, L. Zhu, X. Zhao, L. Yan, and Y. Tian, “Unsupervised deraining: Where asymmetric contrastive learning meets self-similarity,” *IEEE Trans. Pattern Anal. Mach. Intell.*, vol. 46, no. 5, pp. 2638–2657, 2024.

[61] N. Gao, X. Jiang, X. Zhang, and Y. Deng, “Efficient frequency-domain image deraining with contrastive regularization,” in *Eur. Conf. Comput. Vis.*, 2024, pp. 240–257.

[62] G. Wu, J. Jiang, K. Jiang, and X. Liu, “Learning from history: Task-agnostic model contrastive learning for image restoration,” in *AAAI Conf. Artif. Intell.*, 2024, pp. 5976–5984.

[63] D. R. Martin, C. C. Fowlkes, D. Tal, and J. Malik, “A database of human segmented natural images and its application to evaluating segmentation algorithms and measuring ecological statistics,” in *Int. Conf. Comput. Vis.*, vol. 2, 2001, pp. 416–423.

[64] B. Li, W. Ren, D. Fu, D. Tao, D. Feng, W. Zeng, and Z. Wang, “Benchmarking single-image dehazing and beyond,” *IEEE Trans. Image Process.*, vol. 28, no. 1, pp. 492–505, 2019.

[65] W. Yang, R. T. Tan, J. Feng, J. Liu, Z. Guo, and S. Yan, “Deep joint rain detection and removal from a single image,” in *IEEE Conf. Comput. Vis. Pattern Recog.*, 2017, pp. 1685–1694.

[66] S. W. Zamir, A. Arora, S. H. Khan, M. Hayat, F. S. Khan, M. Yang, and L. Shao, “Multi-stage progressive image restoration,” in *IEEE Conf. Comput. Vis. Pattern Recog.*, 2021, pp. 14821–14831.

[67] Y. Cui, W. Ren, X. Cao, and A. Knoll, “Image restoration via frequency selection,” *IEEE Trans. Pattern Anal. Mach. Intell.*, vol. 46, no. 2, pp. 1093–1108, 2024.

[68] X. Chen, H. Li, M. Li, and J. Pan, “Learning A sparse transformer network for effective image deraining,” in *IEEE Conf. Comput. Vis. Pattern Recog.*, 2023, pp. 5896–5905.

[69] Q. Fan, D. Chen, L. Yuan, G. Hua, N. Yu, and B. Chen, “A general decoupled learning framework for parameterized image operators,” *IEEE Trans. Pattern Anal. Mach. Intell.*, 2019.

[70] M. Yao, R. Xu, Y. Guan, J. Huang, and Z. Xiong, “Neural degradation representation learning for all-in-one image restoration,” *IEEE Trans. Image Process.*, vol. 33, pp. 5408–5423, 2024.

[71] S. Nah, T. H. Kim, and K. M. Lee, “Deep multi-scale convolutional neural network for dynamic scene deblurring,” in *IEEE Conf. Comput. Vis. Pattern Recog.*, 2017-07, pp. 3883–3891.

[72] C. Wei, W. Wang, W. Yang, and J. Liu, “Deep retinex decomposition for low-light enhancement,” in *Brit. Mach. Vis. Conf.*, 2018, p. 155.

[73] J. Liang, J. Cao, G. Sun, K. Zhang, L. V. Gool, and R. Timofte, “SwinIR: Image restoration using swin transformer,” in *Int. Conf. Comput. Vis. Workshops*, 2021, pp. 1833–1844.

[74] L. Liu, L. Xie, X. Zhang, S. Yuan, X. Chen, W. Zhou, H. Li, and Q. Tian, “TAPE: task-agnostic prior embedding for image restoration,” in *Eur. Conf. Comput. Vis.*, vol. 13678, 2022, pp. 447–464.

[75] J. M. J. Valanarasu, R. Yasarla, and V. M. Patel, “TransWeather: Transformer-based restoration of images degraded by adverse weather conditions,” in *IEEE Conf. Comput. Vis. Pattern Recog.*, 2022, pp. 2343–2353.

[76] P. Arbeláez, M. Maire, C. Fowlkes, and J. Malik, “Contour detection and hierarchical image segmentation,” *IEEE Trans. Pattern Anal. Mach. Intell.*, vol. 33, no. 5, pp. 898–916, 2011.

[77] K. Ma, Z. Duanmu, Q. Wu, Z. Wang, H. Yong, H. Li, and L. Zhang, “Waterloo Exploration Database: New challenges for image quality assessment models,” *IEEE Trans. Image Process.*, vol. 26, no. 2, pp. 1004–1016, Feb. 2017.

[78] R. Qian, R. T. Tan, W. Yang, J. Su, and J. Liu, “Attentive generative adversarial network for raindrop removal from a single image,” in *IEEE Conf. Comput. Vis. Pattern Recog.*, 2018, pp. 2482–2491.

[79] R. Li, L.-F. Cheong, and R. T. Tan, “Heavy rain image restoration: Integrating physics model and conditional adversarial learning,” in *IEEE Conf. Comput. Vis. Pattern Recog.*, 2019, pp. 1633–1642.

[80] Y. Liu, D. Jaw, S. Huang, and J. Hwang, “DesnowNet: Context-aware deep network for snow removal,” *IEEE Trans. Image Process.*, vol. 27, no. 6, pp. 3064–3073, 2018.

[81] Q. Guan, Q. Yang, X. Chen, T. Song, G. Jin, and J. Jin, “WeatherBench: A real-world benchmark dataset for all-in-one adverse weather image restoration,” in *ACM Int. Conf. Multimedia*, 2025, p. 12607–12613.

- [82] Y. Guo, Y. Gao, Y. Lu, R. W. Liu, and S. He, "OneRestore: A universal restoration framework for composite degradation," in *Eur. Conf. Comput. Vis.*, 2024, pp. 255–272.
- [83] T. Wang, X. Yang, K. Xu, S. Chen, Q. Zhang, and R. W. H. Lau, "Spatial attentive single-image deraining with a high quality real rain dataset," in *IEEE Conf. Comput. Vis. Pattern Recog.*, 2019, pp. 12 270–12 279.
- [84] J. Xiao, X. Fu, A. Liu, F. Wu, and Z.-J. Zha, "Image de-raining transformer," *IEEE Trans. Pattern Anal. Mach. Intell.*, vol. 45, no. 11, pp. 12 978–12 995, 2023.
- [85] R. Li, R. T. Tan, and L.-F. Cheong, "All in one bad weather removal using architectural search," in *IEEE Conf. Comput. Vis. Pattern Recog.*, 2020, pp. 3175–3185.
- [86] Y. Zhu, T. Wang, X. Fu, X. Yang, X. Guo, J. Dai, Y. Qiao, and X. Hu, "Learning weather-general and weather-specific features for image restoration under multiple adverse weather conditions," in *IEEE Conf. Comput. Vis. Pattern Recog.*, 2023, pp. 21 747–21 758.
- [87] O. Özdenizci and R. Legenstein, "Restoring vision in adverse weather conditions with patch-based denoising diffusion models," *IEEE Trans. Pattern Anal. Mach. Intell.*, vol. 45, no. 8, pp. 10 346–10 357, 2023.
- [88] T. Ye, S. Chen, J. Bai, J. Shi, C. Xue, J. Jiang, J. Yin, E. Chen, and Y. Liu, "Adverse weather removal with codebook priors," in *Int. Conf. Comput. Vis.*, 2023, pp. 12 619–12 630.
- [89] Y. Ai, H. Huang, X. Zhou, J. Wang, and R. He, "Multimodal prompt perceiver: Empower adaptiveness, generalizability and fidelity for all-in-one image restoration," in *IEEE Conf. Comput. Vis. Pattern Recog.*, 2024, pp. 25 432–25 444.
- [90] T. Ye, S. Chen, W. Chai, Z. Xing, J. Qin, G. Lin, and L. Zhu, "Learning diffusion texture priors for image restoration," in *IEEE Conf. Comput. Vis. Pattern Recog.*, 2024, pp. 2524–2534.
- [91] S. Sun, W. Ren, X. Gao, R. Wang, and X. Cao, "Restoring images in adverse weather conditions via histogram transformer," in *Eur. Conf. Comput. Vis.*, 2024, pp. 111–129.
- [92] Y. Song, Z. He, H. Qian, and X. Du, "Vision transformers for single image dehazing," *IEEE Trans. Image Process.*, vol. 32, pp. 1927–1941, 2023.
- [93] Y. Zhang, S. Zhou, and H. Li, "Depth information assisted collaborative mutual promotion network for single image dehazing," in *IEEE Conf. Comput. Vis. Pattern Recog.*, 2024, pp. 2846–2855.
- [94] X. Chen, J. Pan, and J. Dong, "Bidirectional multi-scale implicit neural representations for image deraining," in *IEEE Conf. Comput. Vis. Pattern Recog.*, 2024, pp. 25 627–25 636.
- [95] S. Chen, T. Ye, Y. Liu, E. Chen, J. Shi, and J. Zhou, "Snowformer: Scale-aware transformer via context interaction for single image desnowing," *CoRR*, vol. abs/2208.09703, 2022.
- [96] D. Zheng, X. Wu, S. Yang, J. Zhang, J. Hu, and W. Zheng, "Selective hourglass mapping for universal image restoration based on diffusion model," in *IEEE Conf. Comput. Vis. Pattern Recog.*, 2024, pp. 25 445–25 455.
- [97] R. Zhu, Z. Tu, J. Liu, A. C. Bovik, and Y. Fan, "Mwformer: Multi-weather image restoration using degradation-aware transformers," *IEEE Trans. Image Process.*, vol. 33, pp. 6790–6805, 2024.



Gang Wu received the B.E. degree in the School of Computer Science and Technology from Soochow University, Jiangsu, China, in 2020. He is currently pursuing the Ph.D. degree in Faculty of Computing at Harbin Institute of Technology. His research interests include image restoration, representation learning, and self-supervised learning.



Junjun Jiang received the B.S. degree in Mathematics from the Huaqiao University, Quanzhou, China, in 2009, and the Ph.D. degree in Computer Science from the Wuhan University, Wuhan, China, in 2014. From 2015 to 2018, he was an Associate Professor with the School of Computer Science, China University of Geosciences, Wuhan. From 2016 to 2018, he was a Project Researcher with the National Institute of Informatics (NII), Tokyo, Japan. He is currently a Professor with the School of Computer Science and Technology, Harbin Institute of Technology, Harbin, China. His research interests include image processing and computer vision.



Kui Jiang received the M.E. and Ph.D. degrees from the School of Computer Science, Wuhan University, Wuhan, China, in 2019 and 2022, respectively. Before July 2023, he was a Research Scientist with the Cloud BU, Huawei. He is currently an Associate Professor with the School of Computer Science and Technology, Harbin Institute of Technology. He received the 2022 ACM Wuhan Doctoral Dissertation Award. His research interests include image/video processing and computer vision.



Xianming Liu received the B.S., M.S., and Ph.D. degrees in computer science from the Harbin Institute of Technology (HIT), Harbin, China, in 2006, 2008, and 2012, respectively. In 2011, he spent half a year at the Department of Electrical and Computer Engineering, McMaster University, Canada, as a Visiting Student, where he was a Post-Doctoral Fellow from 2012 to 2013. He was a Project Researcher with the National Institute of Informatics (NII), Tokyo, Japan, from 2014 to 2017. He is currently a Professor with the School of Computer Science and Technology, HIT. His research interests include trustworthy AI, 3D signal processing and biomedical signal processing.



Liqiang Nie received the B.Eng. and Ph.D. degree from Xi'an Jiaotong University and National University of Singapore (NUS), respectively. After Ph.D., he continued his research in NUS as a research fellow for three years. He is currently the dean of the Department of Computer Science and Technology, Harbin Institute of Technology (Shenzhen). His research interests lie primarily in multimedia computing and information retrieval. He is an AE of IEEE TIP, IEEE TKDE, IEEE TMM, IEEE TCSVT, ACM ToMM, and Information Science. Meanwhile, he serves as the chair of ICMR 2025, ICME 2025, and ACM MM 2027. He is a member of ICME steering committee. He has received many awards over the past four years, like SIGMM rising star in 2020, MIT TR35 China 2020, SIGIR best student paper in 2021, IEEE AI's 10 to Watch in 2022, ACM MM Best paper award in 2022, and the National Youth Science and Technology Award in 2024.